

ION BEAM ANALYSIS : A CENTURY OF EXPLOITING THE ELECTRONIC AND NUCLEAR STRUCTURE OF THE ATOM FOR MATERIALS CHARACTERISATION

CHRIS JEYNES

*University of Surrey Ion Beam Centre
Guildford GU2 7XH, England
c.jeynes@surrey.ac.uk*

ROGER P. WEBB

*University of Surrey Ion Beam Centre
r.webb@surrey.ac.uk*

ANNIKA LOHSTROH

*Department of Physics, University of Surrey
a.lohstroh@surrey.ac.uk*

Analysis using MeV ion beams is a thin film characterisation technique invented some 50 years ago which has recently had the benefit of a number of important advances. The review will cover damage profiling in crystals including studies of defects in semiconductors, surface studies, and depth profiling with sputtering. But it will concentrate on *thin film depth profiling* using Rutherford backscattering, particle induced X-ray emission and related techniques in the deliberately synergistic way that has only recently become possible. In this review of these new developments, we will show how this integrated approach, which we might call "*Total IBA*", has given the technique great analytical power.

Keywords: RBS, EBS, PIXE, ERD, NRA, MEIS, LEIS, SIMS, IBIC.

1. Introduction

Ion beam analysis is a very diverse group of characterisation techniques which have been applied to every class of material where the interest is in the surface or near-surface region up to a fraction of a mm in thickness. Such a field is far too broad to be reasonably covered by such a review as this; we will concentrate on thin film elemental depth profiling methods using ions with energies of order 1 MeV/nucleon. We will emphasise complementary techniques, including some other closely related IBA¹ methods.

Thin film elemental depth profiling is of critical importance to a wide variety of modern technolo-

gies, including the semiconductor, sensor, magnetics, and coatings industries (including both tribology and optics), among others. It is also valuable in many other disparate applications such as cultural heritage, environmental monitoring and forensics. We will be describing examples in many of these areas in our review of MeV-IBA.

Historically, IBA labs have tended to split into (at least) two "traditions": on the one hand nuclear methods (RBS, ERD, NRA), and on the other atomic methods (PIXE). We will outline various reasons for this, but will show that recent advances have facilitated the integration of these two traditions giving us what is effectively a new and much more powerful technique.

Curiously, this review seems to touch on all the main breakthroughs in 20th century physics, and all IBA techniques hinge on spectroscopy. So perhaps we should start by acknowledging our debt to Isaac

¹ see the end of the chapter for expansion and explanation of acronyms. Appendix A is a glossary of IBA techniques, and Appendix B is a glossary of related techniques.

Newton, who in 1671 was the first to use the word "spectrum" with the modern connotation of *quantum phenomenon observed with a dispersive mechanism* [1]^{II}. Previously (and subsequently) "spectrum" had the connotation of "spectre" or "apparition". But philosophers see reality.

1.1. *Scope of chapter*

Although concentrating on MeV IBA depth profiling, we will mention methods of depth profiling crystallographic defects using channelling and MEIS; characterising defects in semiconductors, including their spacial distribution, by IBIC; and depth profiling using sputtering by SIMS (including MeV-SIMS), although we will not discuss beam damage extensively. We will also mention ion beam methods sensitive to the true surface (MEIS, LEIS) since they also use RBS.

We will not specifically review microbeam applications, taking microbeam technology for granted throughout the text. But it will be clear that we think that 3D spacial resolution is central to the general usefulness of IBA.

1.2. *Complementary techniques*

Throughout, we will also mention complementary techniques wherever appropriate. Materials analysis must be a strongly interdisciplinary field, and the characterisation problems of modern materials almost invariably require the use of a variety of techniques for their solution. Any discussion of a technique without the context of complementary techniques is likely to be strongly misleading.

In all these fields the analyst has various standard tools: the electron microscopies and spectroscopies^{III} (SEM, TEM, XPS, AES and their vari-

^{II} Using Newton's spelling of "phænomenon" which transliterates the Greek φαινόμενον. In his use of "spectrum" Newton had in mind the Latin etymology of *specere*, to see.

^{III} "spectrometry" or "spectroscopy"? A spectrum is the object that results from some dispersive process: we do *spectrometry* where we measure the spectrum and *spectroscopy* where we look at the spectrum. The Hubble red-shift for example is a *spectroscopic* effect since the recognisable pattern of atomic absorption

ants)^{IV}, the scanning probe microscopies (AFM and variants including the new optical near-field methods), X-ray techniques like XRF and XRD (also with many variants) and optical methods like ellipsometry, Raman, FTIR and other spectroscopies. Elemental depth profiling can be done destructively using sputtering techniques with SIMS (or, frequently, AES). If destructive techniques are considered then bulk methods like ICP-MS and AMS should be mentioned, and of course there are a wide variety of wet chemical analytical methods. XRF and XRD are frequently applied to "bulk" as well as thin film samples, and other comparable fluorescence techniques are cathodoluminescence or photoluminescence. Molecular imaging can already be done in air by MALDI, DESI and DART.

Where does IBA fit in this kaleidoscope of techniques? IBA typically uses an accelerator which needs a hall of at least 200m², a footprint well over an order of magnitude larger than any of the other techniques mentioned – it is necessarily a technique with high running costs. What can it do which cannot be done reasonably easily by other techniques? If a materials research organisation (for example, a University) were to set up a central analytical laboratory to service the needs of all its research groups and other collaborators, would IBA be one of the techniques considered "essential"?

We believe that modern integrated IBA methods are exceptionally powerful for a wide range of materials problems, and we will show a number of significant examples that exemplify this.

1.3. *Overview of chapter*

In §§2, 4 we will summarise the nuclear and atomic IBA techniques we will be concentrating on, and in §6 we will address their integration. §3 will

lines has shifted to different frequencies. However, the boundary between spectroscopy (as in XPS) and spectrometry (as in RBS) is ill-defined, and it is mostly a conventional distinction.

^{IV} see Appendix B for a glossary expanding and explaining acronyms for complementary characterisation techniques.

briefly describe the other IBA techniques, for a more complete overview of the field. In §5 we will discuss the important issue of computer codes used in IBA, together with a further discussion of the high accuracy available with these methods.

A general introduction to the field must mention the three IBA Handbooks published over the last 35 years. The 1977 "green book" [2] includes a section on PIXE which was dropped from the more extensive "black book" from 1995 [3]. PIXE is restored in the recent 2-volume Handbook [4]. There have been an almost unbroken series of biennial IBA Conferences, the first of which was held in 1973 [5]. Currently the most recent published Proceedings are from the Cambridge conference in September 2009 [6]: the Proceedings are not yet available from the Brazil conference of April 2011. There is also a triennial PIXE conference series, the latest of which was in Surrey in 2010 [7]. Other useful recent reviews include Giuntini (2011) on the use of external beams [8].

2. Nuclear IBA depth profiling methods

Large angle ion scattering was first observed in Geiger & Marsden's experiments in 1909 [9], which were interpreted by Ernest Rutherford in 1911 to demonstrate the existence of the positively charged atomic nucleus [10]. The transition from RBS to EBS as the Coulomb barrier is exceeded was first demonstrated by Chadwick & Bieler in 1921 (for alphas on H [11]). The wave-mechanical interference between identical scattered and recoil nuclei due to their indistinguishability was pointed out (for electrons) by Mott in 1930 [12] and immediately verified using magnetic spectrometers for proton-proton RBS [13] and EBS (with measurements [14] and theory [15]). Explicit energy spectra were not published until the 1950s (in papers on the quantum mechanical calculation [16] and analytical chemistry [17]). Davies, Amsel & Mayer point out in their nice 1992 "reminiscences" paper [18] that J.O.Nielsen observed a beautifully Gaussian implantation range profile of 40 keV Gd in Al in 1956. But the technique did not become useful for materials analysis until more convenient silicon diode detec-

tors were available, with the first paper by Georges Amsel on Si diode detectors in 1960 [19] and Turkevich's immediate proposal for the Surveyor Moon mission in 1961 [20] with the report in 1967 [21]. Explicit depth profiles were not published until 1970 [22].

2.1. Energy loss

It was obvious to all the early workers that the *energy loss* of scattered particles represented *depth* in the samples, and the famous *Bragg rule* (1905) [23] obtained the compound stopping power for a fast particle from a linear combination of elemental stopping powers.

To interpret IBA spectra in general it is essential to have energy loss ("stopping power") data for the whole periodic table and all the ion beams of interest. This is a massive task both of measurement and of evaluation against a theoretical model. The measurements are difficult to make and the model enables both a valid comparison between different sets and also extrapolation to materials or beams for which measurements are not available. Happily this has been done, with comprehensive stopping power databases now available from Jim Ziegler's SRIM website [24] [25] [26]. Helmut Paul has also recently reviewed this field with references to other compilations (H.Paul [27], MSTAR, ICRU...) [28].

The Bragg rule is an approximation that clearly implies that the inelastic energy loss of an energetic particle is largely due to inner-shell (strongly bound) electrons: otherwise there would be more noticeable chemical effects, which have long been observed (Bourland & Powers, 1971, studied alphas in gases [29]) but are not large. For example, Bragg's rule applies even for heavy ions in ZrO₂ [30] and TiO₂ [31], but ~5% deviations were measured for light ions in polyvinyl formal [32]. Up to 20% deviations can be seen in some cases, and these are discussed in detail in the SRIM 2010 paper [33].

In the following we will assume that the analyst has good stopping power values. However, it must be pointed out that these are basic analytical data, which are not easy to obtain accurately. Therefore

any critical work must take into account the uncertainties deriving from the stopping power database. Both Paul's work cited above and the SRIM database give these uncertainties in considerable detail: as a rough indication for the reader, a stopping power value is unlikely to be known much better than about 4%.

2.2. Rutherford backscattering spectrometry

Rutherford reasoned that the scattering of positively charged alpha particles must be due to the Coulomb repulsion of a (positively charged) atomic nucleus. He therefore derived the simple relation for the differential scattering cross-section $d\sigma/d\Omega$:

$$d\sigma/d\Omega = \{ Z_1 Z_2 e^2 \operatorname{cosec}^2(\theta/2) / 4E \}^2 \quad (1)$$

where $d\Omega$ is the solid angle at the detector, θ is the angle of scattering, E is the particle energy at scattering, Z_i are the atomic numbers of the projectile and target nuclei and e is the charge on the electron. This formula was verified in detail by Geiger & Marsden in 1913 [34].

For simplicity, Eq.1 is written in the *centre-of-mass frame of reference* and therefore has no mass dependence: in the *laboratory frame* it is rather more complicated, usefully given in a power series by Marion & Young [35]:

$$d\sigma/d\Omega \cong \{ Z_1 Z_2 e^2 / 4E \}^2 \{ \sin^{-4}(\theta/2) - 2r^{-2} + \dots \} \quad (1a)$$

$$r \equiv M_2 / M_1 \quad (2)$$

where M_1 and M_2 are the masses of the incident and target nuclei respectively.

The Rutherford formula is derived from the Coulomb repulsion of two like charges assuming that the two colliding nuclei are bare point charges. The electron screening that must shield the charges from each other until the nuclei are in very close proximity is usually rather a small effect which was determined in adequate detail by Andersen *et al* in 1980 [36]. It is this screening correction that relieves the singularity at $\theta = 0$ where Eq.1 makes the cross-section infinite: with no scattering the nuclei are so far apart that the nuclear charge is screened by the electron shells, and the cross-section vanishes.

The scattering event itself must conserve energy and momentum, and thus for an elastic scattering event the *kinematics* give the split of the initial energy E_0 between the scattered and the recoiled nuclei:

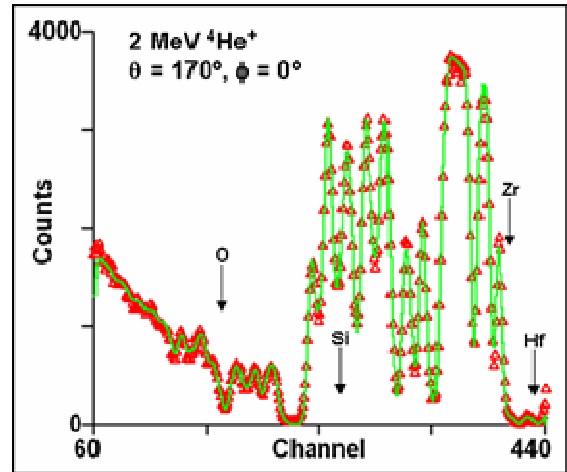
$$E \equiv kE_0 \quad (3)$$

$$k_s = \{ (\cos \theta \pm (r^2 - \sin^2 \theta)^{1/2}) / (1 + r) \}^2 \quad (4)$$

$$k_r = (4r \cos^2 \phi) / (1 + r)^2 \quad (5)$$

where k is known as the "kinematical factor" given (in the laboratory frame) for the scattered particle (Eq.4) with a scattering angle of θ , and the recoiled particle (Eq.5) with a recoil angle of ϕ . The scattering and recoil angles are measured relative to the incident beam direction. Eq.4 is double-valued if $r < 1$; for $r > 1$ the positive sign is taken. Thus, for a head-on collision with $r > 1$ (e.g., He RBS), $\theta = 180^\circ$ and $k_s = \{(M_2 - M_1) / (M_2 + M_1)\}^2$. In the case $r < 1$ (ERD), there can be no scattering into angles $\theta > \sin^{-1} r$. Note that the kinematical factor is *not* a function of beam energy: RBS spectra look qualitatively similar for all beam energies.

Figure 1. Antireflection coating with alternate zirconia and silica layers on float glass. Normal incidence beam: the line through the points is the spectrum calculated for the fitted structure. The surface positions of Hf, Zr, Si, O are shown. Hf is a normal contaminant in Zr. (From Fig.2 of Jeynes *et al*, 2000 [37]).



We can now give an example of RBS analysis. Fig.1 shows the RBS spectrum from an antireflection coating on a glass substrate, where the coating is about a micron thick: the detailed analysis fits 19 alternating layers of zirconia and silica,

where these molecules and the substrate are treated as three *logical elements* for fitting purposes [37]. Notice that the fit (the line through the data points) is extremely good: this means that the model for the fitting is also very good, in fact, the layer thicknesses are determined with *sub-nm precision* even at the bottom of the coating (for details see the paper). We will discuss this exceptional precision below (§5.4).

2.3. Elastic (non-Rutherford) backscattering

Figure 2. "S-factor" calculated from the AZURE fit to the $^{12}\text{C}(p,\gamma)^{13}\text{N}$ data of J.Vogl (PhD Thesis, Cal.Tech., 1963) (and using the $^{12}\text{C}(p,p)^{12}\text{C}$ data of Meyer *et al*, 1976: see IBANDL at www-nds.iaea.org/ibandl). The red (solid) line indicates the best fit including external capture, which the blue (dashed) line neglects (reproduced from Fig.3 of Azuma *et al*, 2010 [40]). Note that the S-factor is significant right down to zero energy.

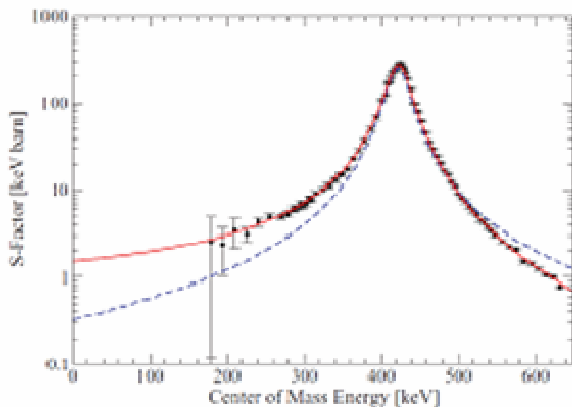
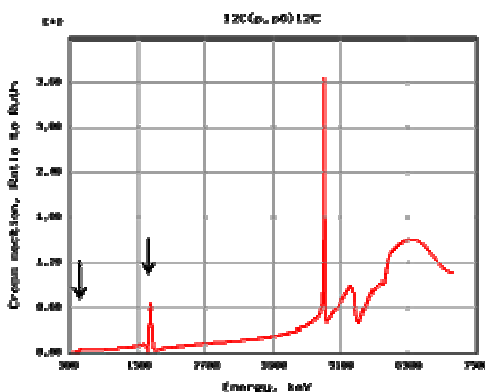
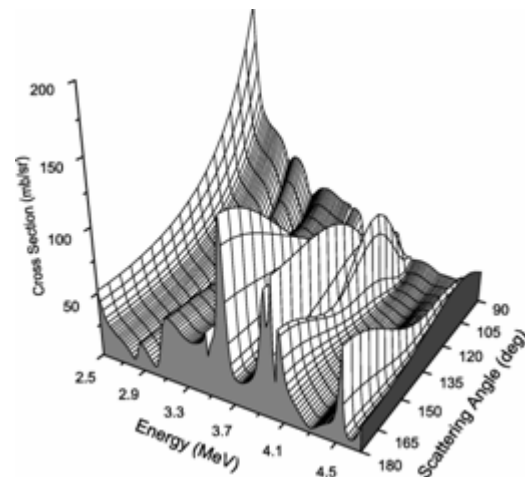


Figure 3. Evaluated $^{12}\text{C}(p,p)^{12}\text{C}$ elastic scattering cross-section for $\theta=180^\circ$, relative to the Rutherford cross-section, by Gurbich & co-workers [40]. Note the resonances at 440 keV and 1734 keV (arrowed). Downloaded 21 July 2011 using the SigmaCalc calculator at www-nds.iaea.org/ibandl.



As the beam energy is increased, Rutherford's approximation of point charges for the colliding nuclei fails, the Coulomb barrier is exceeded, and a proper quantum mechanical treatment of the interaction must be made. An estimate of the "Actual Coulomb Barrier" was made using optical model calculations by Bozoian *et al* [38] (Appendix 8 of both Handbooks [3] [4]) but the optical model does not take into account specific features of nuclei (apart from the radius, A and Z) and the "Coulomb barrier" is not an identifiable potential useful for calculation [39]; this is emphasised by the calculations of the astrophysicists who calculate the probability of (p,γ) reactions at *stellar* temperatures ($\sim 10\text{--}30$ keV!).

Figure 4. Evaluated $^{14}\text{N}(\alpha,\alpha)^{14}\text{N}$ cross-sections as a function of scattering angle, reproduced from Fig.4, Gurbich *et al*, 2011 [46].



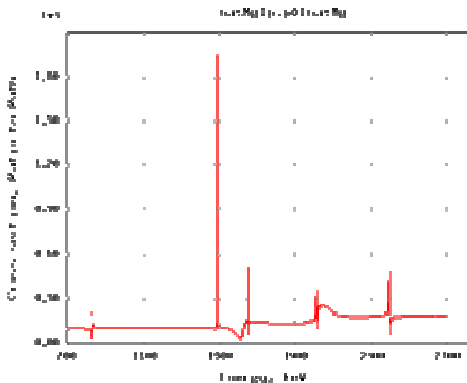
For example, the $^{12}\text{C}(p,\gamma)^{13}\text{N}$ reaction is critical to understanding stellar hydrogen burning in massive stars, initiating the CNO cycle. Fig.2 shows the "S-factor" for this reaction^V, near the resonance at 461 keV (centre of mass frame), which is also observable in the elastic scattering $^{12}\text{C}(p,p)^{12}\text{C}$ reaction channel at 440 keV (laboratory frame: see Fig.3 [40]). This S-factor is calculated using the AZURE code of Azuma *et al* [41]. The S-factor is the pre-factor in the expression for the cross-

^V The ordinate in Figs.2, 4, 26 is in "barns" $\equiv 10^{-24}\text{cm}^2$. The word "barn" (as in large farmyard building) is a joke of the nuclear physicists, and according to the Oxford English Dictionary first used by Holloway & Baker in 1942

section which has an (approximately) exponential decrease with energy corresponding to the term for tunnelling through the Coulomb barrier. The point is that these cross-sections are dominated by the low energy tails of the resonances due to the nuclear structure.

These complicated elastic scattering cross-section functions can be calculated from nuclear models, using all available nuclear data (not only scattering cross-section data). We have already mentioned the AZURE code (see Fig.2). The materials community, under the auspices of an IAEA CRP [42] has built the IBANDL website (www-nds.iaea.org/ibandl) which gathers together all the relevant cross-section measurements available [43]. IBANDL also gives access to the SigmaCalc calculator (www-nds.iaea.org/sigmacalc) of Gurbich [44] [45] which is based on several codes in which various nuclear reaction models are implemented, the calculations being performed with individual sets of parameters obtained through the evaluation procedure for each reaction considered. These nuclear models have been used to critically *evaluate* existing elastic scattering (and other) cross-section measurements, enabling nuclear parameters to be chosen such that the cross-section can be calculated for any scattering angle with a much smaller uncertainty than for any particular dataset.

Figure 5. SigmaCalc calculation of $^{nat}\text{Mg}(p,p)^{nat}\text{Mg}$ elastic scattering cross-section (relative to Rutherford) for $\theta=180^\circ$ [47]. Downloaded 21 July 2011 from www-nds.iaea.org/ibandl.

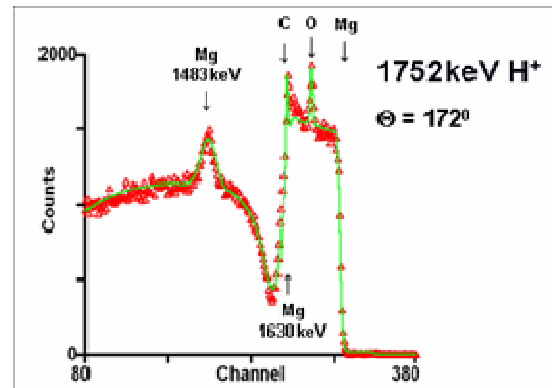


As an example, Fig.4 shows the strong angular dependence of the $^{14}\text{N}(\alpha,\alpha)^{14}\text{N}$ reaction [46]. It is

clear that, were a nuclear model not available, the experimenter would have to rely on measured cross-sections only, and would be forced either to make measurements for the experimental geometry used, or set the scattering angle to match the existing measurements.

Fig.5 shows the evaluated elastic scattering cross-sections for protons on natural magnesium, relative to Rutherford, with a benchmark measurement shown in Fig.6 [47]. Note the exceptionally strong and sharp resonance at 1483 keV. It is not trivial to calculate spectra which involve cross-sections with such sharp resonances, and special methods need to be used [48].

Figure 6. Benchmark EBS measurement of bulk magnesium showing strong resonances at 1483 and 1630 keV (from Fig.3 of Gurbich & Jeynes, 2007 [47]). An O peak from the surface oxide and a C peak from surface contamination are visible.



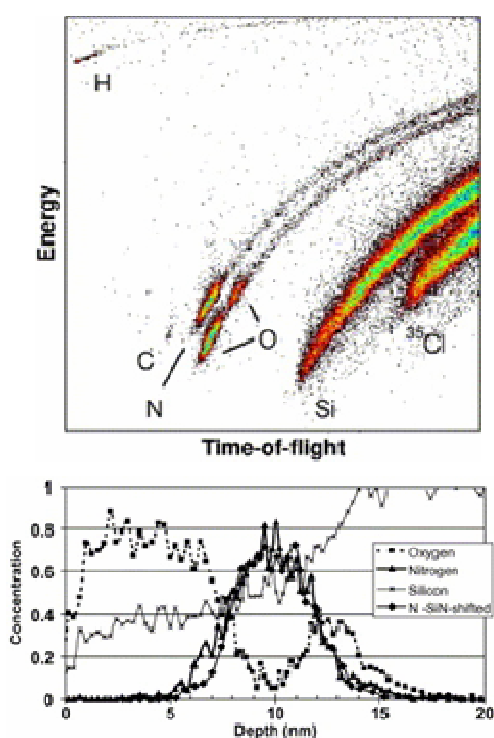
For both ^{12}C and ^{nat}Mg elastic scattering (p,p_0) cross-sections, optical model estimates of the "actual Coulomb barrier" energy are wildly wrong, as expected [39], and as is clear from Table 1 which gathers available data together to estimate the minimum beam energy where the (p,p) cross-section differs significantly from Rutherford: the value of 4% deviation is chosen because it is not presently possible to specify the value at 1% (or even 2%) deviation with any confidence.

2.4. Elastic recoil detection

Eq.5 shows the kinematical factor for the recoil ion in the scattering event. In every elastic scattering event the kinematics requires that the target atom is

recoiled with significant energy. If the target is thin, or the geometry is appropriate, such a recoil particle could escape the sample and be measured.

Figure 7. 6 MeV ^{35}Cl ToF-ERD analysis of a 15 nm 3-layer oxide/nitride stack (SiO_2 8nm / Si_3N_4 5nm / SiO_2 2nm / Si substrate). The analysis is repeated with the surface oxide etched off. *Above:* Time of flight spectra with 38.2° detector angle and 3.6° exit (beam take-off) angle. Both scattered ^{35}Cl and recoiled Si, O, N, C and H can be seen. *Below:* Reconstruction of depth profile for unetched and etched samples. The N profile for the etched sample is marked "shifted" and aligns with original N profile. Reproduced from Figs.1&2 of Brijs *et al* (2006) [53].

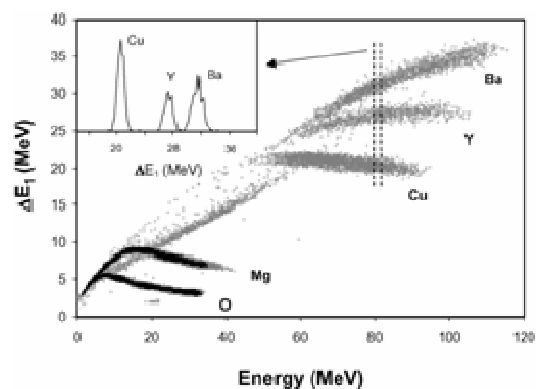


The earliest example of ERD, from the Montréal group in 1976, used a transmission target and a normally incident 35 MeV ^{35}Cl beam to detect Li recoiled from a LiF target [49], obtaining a depth resolution of $24 \mu\text{g}/\text{cm}^2$ of copper. In 1998 Dollinger *et al* [50] used a 60 MeV $^{127}\text{I}^{23+}$ beam on a thick HOPG^{VI} sample tilted at $>85^\circ$ to the beam and a recoil angle of 10° , and energy analysed recoiled $^{12}\text{C}^{5+}$ ions with a magnetic spectrograph. They were able to distinguish the first four or five atomic

^{VI} HOPG: highly oriented pyrolytic graphite

layers, but noticed that the HOPG damaged rapidly under the beam with a sputter yield of 500/ion. This analysis gave a depth resolution of $73 \text{ ng}/\text{cm}^2$ of C. There are many subtleties of this complex measurement, which have been analysed in detail by Szilágyi [51]. One good reason for the growing interest in much lower energy beams for ERD is specifically that they are much less damaging, and the prospects for low energy ERD are reviewed by Döbeli *et al* (2005) [52].

Figure 8. 241 MeV ^{197}Au ERD of YBCO/MgO using a gas ionisation (E- ΔE) detector. The scattered Au signal is kinematically forbidden. Reproduced from Fig.3 of Timmers *et al* (2000) [61].



Because ERD typically (with thick targets) uses glancing beam incidence and glancing recoil exit angles, the resultant energy spectra have a significant component of plural scattering events. These will be considered in more detail in §5, but simple single scattering calculations that have dominated the interpretation of IBA data last century are not accurate enough to account for the detail of most ERD spectra. Fig.7 shows ERD from a study comparing the best depth resolution available from a ToF-ERD^{VII} system using a 6 MeV ^{35}Cl beam, with high resolution SIMS and high resolution RBS (using a magnetic spectrometer) [53]. With ToF-ERD a low energy beam is preferable since then the flight time is long compared to the time resolution of the system. This 2006 study highlights the need to interpret ERD spectra more closely,

^{VII} ToF: "time of flight": in this case the "spectrometer" has a flight tube (the "telescope") with a foil at the entrance that the particle must pass through, thus giving a "start" signal, and a detector at the end which gives a "stop" signal.

taking plural scattering properly into account. It shows that the apparent resolution of the N signal does not behave simply since it does not look significantly worse for a buried layer. However, a depth resolution <1 nm is readily available near the surface.

Detectors for ERD pose interesting problems. The ubiquitous Si diode detectors work, but their energy resolution gets much worse for heavy recoil ions. Unfortunately, they are also susceptible to radiation damage, so for heavy ions they don't work for long! Si detectors have the great virtue of simplicity, but they have to be used with a so-called "range foil" to range out the forward scattered (relatively heavy) beam, and therefore simple range foil ERD has two major disadvantages: the loss of energy resolution due to the energy straggle and thickness inhomogeneity of the range foil [54], and the intrinsic indistinguishability of the signals for the various different recoiled target elements. Contrast this with both of Figs.7&8 where the detector distinguishes the different elements.

Nevertheless, for many purposes, especially H-isotope analysis (for which a He or Li beam is ideal: following a proposal in 2000 [55] there were *two* round robin reports in 2004 [56][57]), range foil ERD with a Si detector remains very convenient and powerful. It is worth underlining the value of He-ERD for profiling H isotopes. Hydrogen is difficult to analyse with other methods, and it is a very important element in materials science. He-ERD was developed [58] and optimised [59] very early for H-profiling; it can very easily be used self-consistently with RBS to solve complex materials problems such as the formation of a-GaN by implantation of Ga into SiN_x:H [60].

ToF-ERD does not have the same problems, but (as with every telescope detector) the throughput is limited since there should only be one ion in the detector at a time; of course the longer the detector is, the better the time resolution – equivalent to energy resolution. Gas ionisation detectors have a very long history, and have also been highly developed for ERD. They have the huge advantage that they are completely impervious to beam damage, since the gas can be changed continuously. Fig.8 shows the E- ΔE signal for such a detector using 241

MeV ¹⁹⁷Au ERD of a superconducting YBa₂Cu₃O_{7.8} film on a MgO substrate [61]. The scattered Au signal is forbidden since for this detector angle the solution of Eq.4 is imaginary.

The energy resolution of gas ionisation detectors has always been limited by the entrance window, which needs to be strong enough to withstand the (usually) atmospheric pressure of the gas. Recently, ultra-thin silicon nitride windows have been introduced, together with dramatic simplifications in the design which have been demonstrated to be nearly as good as more complex designs for low energy ERD [62]. These detectors can also be used for heavy-ion RBS, and have an energy resolution better than that of silicon for beams heavier than He. For He the resolution is comparable. Not only can these detectors support a very high count rate, they are also insensitive to light making them usable at high temperatures.

Finally, we should mention the ultimate sensitivity for hydrogen of $< 5.10^{16}$ H/cc in polycrystalline diamond, obtained at the 15 MV superconducting tandem SNAKE^{VIII} facility in München [63]. This was on diamond slices 55 μ m thick using a 17 MeV H⁺ microbeam and detecting H forward recoils and H forward scatters in coincidence. In a 3-D analysis they were able to demonstrate that H was located (in very low concentrations!) at grain boundaries. Note that the forward recoils are indistinguishable from the forward scatters, and this gives the Mott quantum interference term to the scattering cross-section function [12].

Nuclear reaction analysis

Ernest Rutherford first observed nuclear reactions, using the 4.87 MeV α particle from ²²⁶Ra on nitrogen gas: the ¹⁴N(α ,p)¹⁷O reaction has a Q-value of -1.19 MeV, so fast protons were visible [64] [65].

^{VIII} SNAKE: Superconducting Nanoscope for Applied nuclear (KErn-) physics. This pp coincidence technique has to take account of the quantum mechanical indistinguishability of the two protons: the interference effects significantly change the differential scattering cross-sections (see Mott, 1930 [12])!

Later, Cockcroft and Walton were the first to use an accelerator for nuclear reactions, demonstrating the ${}^7\text{Li}(p,\alpha){}^4\text{He}$ reaction [66] (for which the Q-value is 17.347 MeV) which has a non-zero cross-section down to very low energies (0.27 mb/sr at 430 keV [67]). The so-called "Q-values" of these reactions are determined by the mass differences, and can readily be calculated [68] using Einstein's $E=mc^2$ relation.^{IX}

Figure 9. Determination of oxide growth mechanism by NRA. Narrow resonance nuclear reaction profiling using the ${}^{18}\text{O}(p,\alpha){}^{15}\text{N}$ resonance at 151 keV of SiO_2 films on SiC and Si. Oxidation was started in ${}^{16}\text{O}$ and then completed in ${}^{18}\text{O}$. The ${}^{18}\text{O}$ migrates to the surface and the interface during oxidation. The numbers on the figure show the areas under the peaks. Reproduced from Vickridge *et al* (2002), Fig.2 [69]

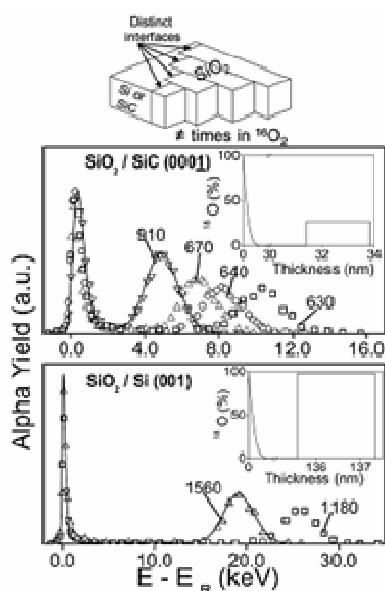


Fig.9 shows an interesting example of the use of NRA methods to determine growth mechanisms. In this case the ${}^{18}\text{O}(p,\alpha){}^{15}\text{N}$ reaction was used near the extremely sharp resonance at 151 keV [69]. Note that sharp resonances allow very high depth resolu-

^{IX} The notation (for example) ${}^{18}\text{O}(p,\alpha){}^{15}\text{N}$ means that a proton ("p") beam is used; it strikes target atoms ${}^{18}\text{O}$; the reaction annihilates the proton which combines with the ${}^{18}\text{O}$ to form ${}^{19}\text{F}$ in an excited state; the excited ${}^{19}\text{F}$ relaxes by splitting into an alpha particle and ${}^{15}\text{N}$, together with 3.98 MeV of energy (the "Q-value") which is split between the resultants using kinematics (conservation of energy and momentum). Thus, the alpha comes off very fast and can readily be recognised and counted.

tion near the surface. The beam energy is varied to collect an "excitation curve": this puts the resonance at various depths in the sample given by the energy loss, and the depth profile can then be reconstructed.

A similar analytical problem involved the tribology (wear resistance) of low-carbon steels, for which nitrogen ion implantation is used. To profile ${}^{15}\text{N}$ implanted into spherulitic cast iron (with heat treatment) the ${}^{15}\text{N}(p,\alpha\gamma){}^{12}\text{C}$ reaction at the strong 898 keV resonance was used [70]. In this case the γ -rays were counted. This material is inhomogeneous both laterally and in depth, being full of graphite nodules. The analysis used a microbeam to profile nitrogen separately in the nodules and in the iron matrix (awkward, since because of the large chromatic aberration of the focussing lenses, every energy change required the beam to be refocussed). This showed that although N is mobile in Fe, it is relatively immobile in C.

There are many nuclear reactions that can be used. Both particle and photon reaction products are available, and cross-sections for these reactions can be calculated using optical model or R-matrix methods. Some evaluated (d,p) and (d, α) reactions can already be found in IBANDL, and some (p, γ) reactions have also been analysed. Of course, measured cross-sections can be used for analytical purposes, or reference standards can be used for relative measurements. The IAEA has established a new CRP to create a database for PIGE [71] as it has already done for EBS [42].

3. Other IBA methods

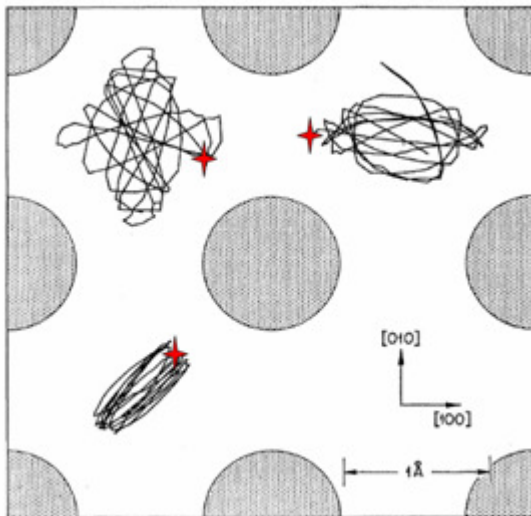
Ion beam methods are not only used for thin film depth profiling, and depth profiling itself comes in various flavours. In this section we will (too briefly, alas) review a variety of other major techniques that should not be ignored.

Methods are available to investigate various aspects of crystals including: lattice site location and damage, and the true structure of the surface (using ion channelling, see §3.1, §3.3); and electrically active defects (using ion beam induced charge measurements, see §3.5).

Low energy beams (requiring completely different detectors) can be used for sensitivity to the true surface (LEIS, see §3.2), and a sensitivity to the first few atomic layers (MEIS, see §3.3). These low energy RBS techniques can also be used for ultra-high resolution thin film depth profiling.

Depth profiling itself is regularly done today with a low energy sputtering ion beam (SIMS, see §3.4). We briefly review this important IBA topic even though the main focus of the present work is MeV-IBA. SIMS is important, not only because it is a standard and widespread technique but because MeV-SIMS is a very interesting new technique giving molecular information that may prove as powerful as MALDI.

Figure 10. Projection of 3 calculated trajectories of 1 keV Cu incident (at points marked with stars) along the $\langle 001 \rangle$ direction of a face centred cubic Cu crystal. The trajectories for 250 collisions are shown and the truncated Bohr potential is used. Reproduced from Fig.2 of Robinson & Oen 1963 [76].

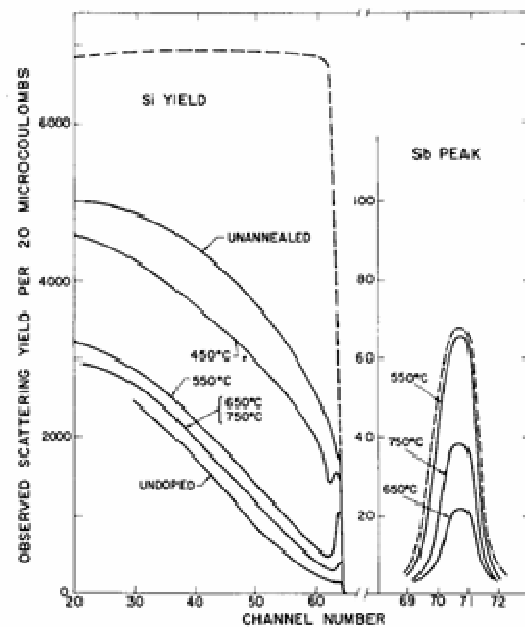


3.1. Crystalline damage and impurities

If an energetic ion beam is aligned with a major axis of a crystal it will "see" a significantly lower stopping power in the so-called channels between the strings of atoms. Moreover, a slightly misaligned beam will experience a *focussing effect* which tends to keep it in the crystal channel. It is this focussing effect that is called **channelling**. Stark & Wendt suggested the existence of this effect in 1912 [72], but Davies, Amsel & Mayer

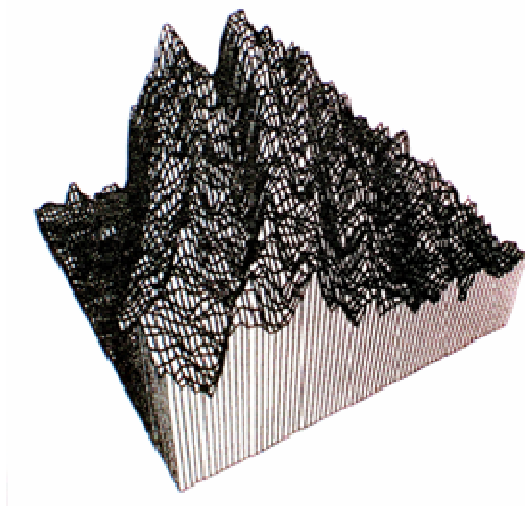
tell us [18] that it was first observed by Bredov & Okuneva in 1957 [73], but they didn't recognise it, misinterpreting their data. It was in 1963 that the first channelling measurements were published by Davies and co-workers [74], who observed the exponential channelling tails of the implant profiles of 210 keV ^{222}Rn in polycrystalline Al by using the alphas emitted by the implanted radon.

Figure 11. 1 MeV proton RBS of $10^{15}\text{Sb}/\text{cm}^2$ implanted at 40 keV into silicon and annealed at various temperatures. Channelling (in $\langle 111 \rangle$ direction) and non-aligned spectra are shown. Reproduced from Fig.1 of Eriksson, Davies, Mayer *et al.*, 1967 [75].



Robinson & Oen's Monte Carlo calculations of the channelling effect also published in 1963 [76] showed that the exponential implant tails were expected. Fig.10 very clearly demonstrates the focussing effect of the channels in a crystal for low energy (1 keV) incident Cu atoms. In non-aligned directions, such an energetic beam would normally have a range of 1.2 nm, but the trajectories shown in this figure have a range of about 30 nm. Knowledge of the energy loss of ion beams channelling in single crystals is important when the depth distribution of impurities and defects is of interest, and this was explicitly considered by Kótai in 1996 [77].

Figure 12. Image (about 3 mm square) of circular damage tracks in a silicon sample turned on a lathe. 1.2 MeV $^4\text{He}^+$ channelled normal to the sample and focussed to a 40 μm spot. Signal is the low-energy part of the RBS Si signal: high yield means high damage. 128x128 pixels, 0.15 nC/pixel, pixel area (23.4 μm)². Reproduced from Fig.4 of Jeynes *et al.*, 1996 [85]



Lindhard published his complete theoretical treatise on channelling in 1965 [78] but it was in 1962 that channelling experiments were first done using all three major IBA techniques: NRA, RBS and PIXE. Blocking was also demonstrated in 1962 to validate Lindhard's reversibility theorem between channelling and blocking. Channelling found an immediate use in the investigation of semiconductor doping by ion implantation and annealing. Fig.11 shows an early measurement of this annealing process.

There is now a very large literature on channelling (see Handbooks). As an indication of the range of possibilities we mention : channelling to determine the defect profiles and defect type in a study of implanted CdTe [79] with quantitation by the code DICADA (see [80] for recent development of this code); also lattice site location of Ni (at low concentration <5 mg/kg) in diamond by PIXE channelling [81]. Monte Carlo codes for channelling include FLUX [82] and CASSIS [83]. RBX is an analytical general purpose IBA code that also able to calculate defect depth profiles and simulate channelled spectra [84].

Fig.12 shows an image of the spatial distribution of crystalline damage in silicon turned on an

ultra-stiff lathe by a single-point diamond tool, where a scanning microbeam is used to form the image [85]. In this case channelling conditions were maintained over the scan area by rocking the beam about the principal axis of the Russian quadruplet focussing magnet using a dog-leg electrostatic scanner before the magnet. Different depths of cut can be seen on the image: in this work amorphous layers up to 350 nm thick are observed, together with dislocation arrays of about $5.10^{10}/\text{cm}^2$ under the amorphous region (quantified with the DICADA code). This is an example of *plastic* deformation in a *brittle* material.

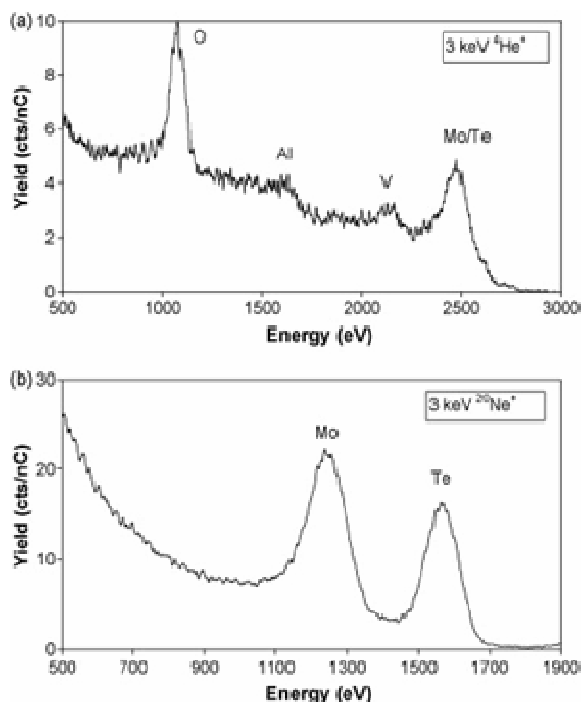
3.2. Catalysis and related studies (LEIS)

RBS spectra can still be obtained for very low energy ion beams of a few keV; this is now called "low energy ion scattering". LEIS was first shown to be a technique selectively sensitive to the true surface (the outermost atomic layer) in 1971 [86]. In this sort of analysis one must use electrostatic detectors, which rely on ion focussing in electric fields, instead of semiconductor diode detectors sensitive to energy loss. Historically, rather simple detectors were used which had a low effective solid angle: thus counting times were relatively long and beam damage severely limited the usefulness of the technique. But in 1992 an efficient electrostatic detector called EARISS^x was reported with orders of magnitude better sensitivity [87] [88]. This has enabled the rapid development of a technique very powerful in applications which require knowledge of the true surface (the outer atomic layer).

Fig.13 shows typical LEIS spectra, using the high sensitivity detector, from a simple recent overview aimed at catalysis applications [89]. The well defined peaks have an area proportional to the number of scattering centres in the outermost atomic layers, and the collection times for these spectra was only a few minutes, giving minimal beam damage (sputtering only <1% of the outermost monolayer).

^x EARISS: energy and angle resolved ISS

Figure 13. LEIS of a mixed oxide catalyst using a beam of 3 keV He⁺ (*above*) and 3 keV Ne⁺ (*below*). The well-defined peaks are from single scattering events at the outer atomic layer. The heavier Ne⁺ beam has mass resolution for Mo/Te but is not sensitive to the light O. Reproduced from Fig.2 of ter Veen *et al* (2009) [89]



3.3. Surface reconstruction studies (MEIS)

The FOM group in Amsterdam developed medium energy ion scattering in the 1970s, as a development of the channelling science worked out in the 1960s [90]. They realised that the details of the scattering would give valuable information about surface relaxation effects in crystals. In particular, LEED data for Cu, Ni and Al crystals were ambiguous and appeared to contradict theory, and another experimental probe was sought.

The low energy LEIS signal in Fig.13 is due to more complex scattering events. LEIS necessarily uses an *electrostatic* detector, which means that the detected species must be an *ion*. Therefore the details of the neutralisation and re-ionisation of the scattered particles are essential to the technique. These have been comprehensively reviewed recently by Brongersma *et al*, 2006 [91]. It turns out that the observed fact that there usually appears to

be little or no matrix effect on the binary collision peak area (for a comprehensive list of literature on this see Table 9.1 of [90]) is rather surprising and is still not well understood. Nevertheless, the behaviour of the LEIS signal *is* well-understood in a wide variety of applications. Noble gas primary ion beams are used because they are readily neutralised in sub-surface interactions, and hence give well-defined binary scattering peaks.

Figure 14. Shadow and blocking cones typical of 200 keV proton MEIS. Reproduced from Fig.19 of Turkenburg *et al*, 1976 [91]

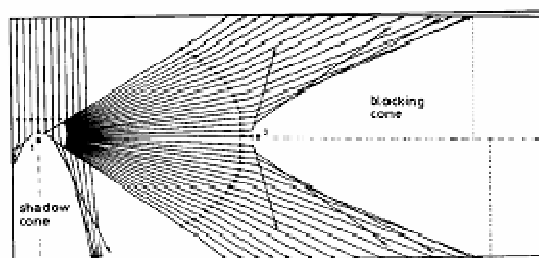
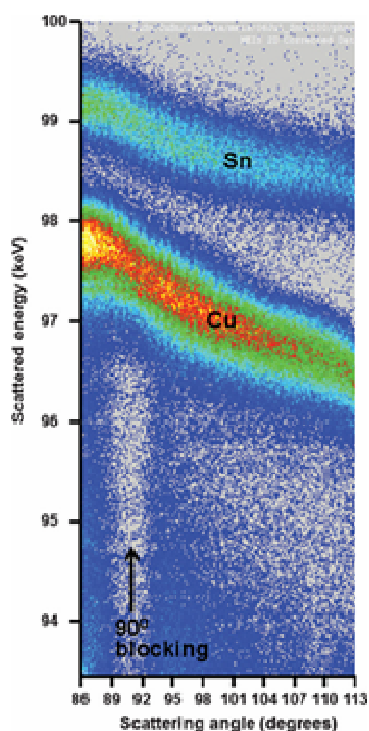


Fig.14 shows the shadow cone for an incident beam entering from the top (left) and passing close to a scattering centre (#1). The scattered beam will in its turn be blocked by a second scattering centre (middle; #2). The blocking and shadow cones are different phenomenologically – it is the blocked beam that is detected, and therefore the detected beam will have low yields in the blocked directions. There is also a real difference, since the shadow cone is for a parallel beam, where the blocking cone is for a beam scattered from a scattering centre that is close. But both effects rely for their detection on atomic coordination given by the crystal symmetry. The authors make it clear, for example, that there will be yield from the atoms near the surface which, relative to the beam, shadow the coordinated strings of atoms behind them, whereas no yield is expected from the shadowed strings. But the blocking effects give valuable information about correlations in the surface as well.

Fig.15 shows a recent example of a joint MEIS/LEIS study of the position of Sn atoms on the surface of Cu crystals, and the rearrangement of the Cu atoms that this implies [92]. Both MEIS

and LEIS (CAICISS) are needed to resolve this complex structure; and AES with LEED are used in both instruments as monitors of, respectively, surface cleanliness and Sn deposition thickness.

Figure 15. MEIS of 100 keV He incident in the $\langle 112 \rangle$ direction on a (100) surface of a Cu crystal with sub-monolayer Sn coverage. The surface signals of the Cu and the Sn overlayer are marked, as is the blocking dip for 90° scattering. Reproduced from Fig.3 of Walker *et al.*, 2011 [92]



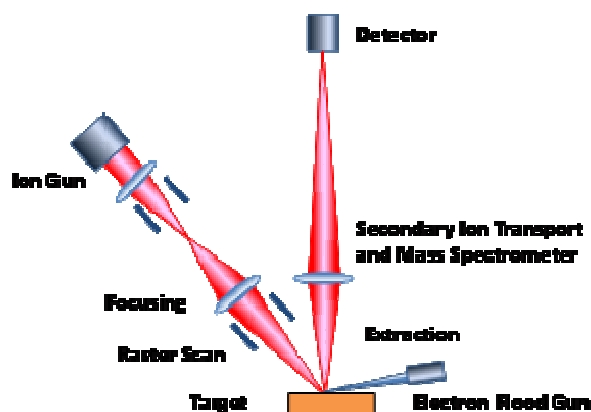
3.4. Sputtering methods (SIMS)

Secondary Ion Mass Spectrometry (SIMS) uses energetic ions to sputter the surface material from a sample. The ejected material is collected with the aid of a mass spectrometer to determine the constituent make-up of the sample.

Fig.16 sketches a SIMS tool: this technique has been well established for three decades [93] but is still under vigorous development. In particular, high throughput ToF instruments [94] are becoming available with a continuous primary beam and a pulsed spectrometer [95]. Other recent work includes complementary SIMS/LEIS to effectively follow the operation of electrochemical systems

(eg: fuel cells!) by isotope exchange depth profiling [96], ultra-low energy SIMS for reliable depth profiling close to the surface (in this case for the tarnishing of silver coating layers on cultural heritage samples) [97], and high resolution EELS analysis of an adhesion problem to complement previous (inconclusive) ToF-SIMS work [98].

Figure 16. Simple schematic of a SIMS system. The scanning ion beam (typically 250 eV – 40 keV O^- or Cs^+) sputters the target. Sputtered ions are extracted into the MS (quadrupole or magnetic sector or ToF are used). The electron flood gun is used for charge compensation of insulating samples.

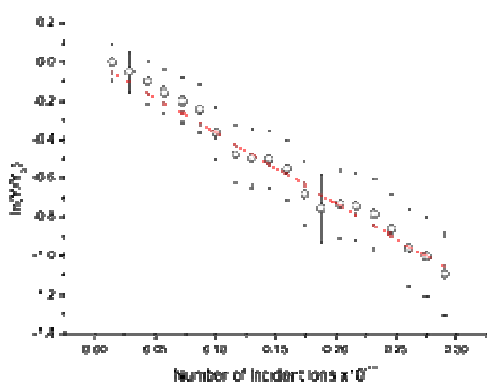


Static SIMS is a surface-sensitive technique where the primary ion fluence is kept below the *static limit*; the fluence at which less than 10% of the surface atoms have been displaced by the primary ion beam, typically less than about 10^{12} ions/cm², ensuring that the signal is from undamaged material. In *Dynamic SIMS* the sample is eroded by the sputtering beam and the mass spectra are recorded as a function of time, giving the elemental depth profile. Some molecular depth profiling is also available since sputtered ions show a molecular fragmentation pattern characteristic of the target. Some SIMS systems have been developed with both high flux (dynamic) and low flux (static) ion guns.

SIMS is not usually a fully quantitative analytical technique because the ionisation probability of the sputtered particles can vary by *orders of magnitude*, depending on the details of the surfaces. Moreover, not only are sputter rates for dynamic SIMS strongly composition-dependent, but also

there are a variety of sputtering artefacts that can significantly modify the composition of the instantaneous surface. These problems are all particularly acute at interfaces. However, the SIMS community has succeeded in full quantification (with reference to certified standards) for many important materials systems.

Figure 17. The natural log of the normalized yield of the protonated leucine ions (132 amu) plotted as a function of the total number of incident ions (10 MeV $^{16}\text{O}^{4+}$). Reproduced from Fig.1 of Jones *et al* (2011) [106]

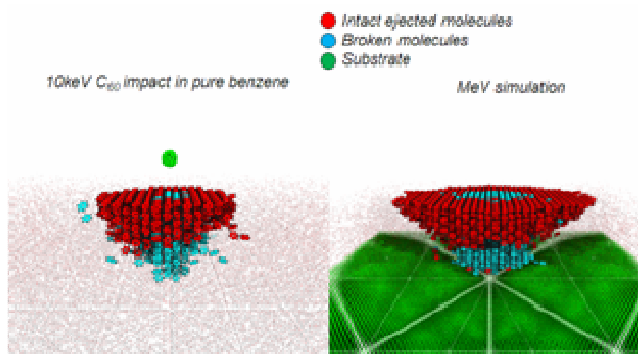


A number of variations of the SIMS technique are in use to increase the fraction of secondary ions or to analyze all of the sputtered particles. Matrix Assisted SIMS uses a matrix (as MALDI – see below) to substantially increase the sputtered ion fraction. Meta-SIMS uses metallic nanoparticles deposited on the surface to again enhance the yield of ionized particles emitted. Secondary Neutral Mass Spectrometry (SNMS) uses a post-ionization chamber to ionize the neutrals sputtered from the surface. There are many more variants and combinations which are not really the focus of this chapter and the interested reader is directed to the various review articles and conference proceedings available: see for example the excellent old review of depth-profiling SIMS from 1982 [99], a recent review of depth-profiling SIMS using molecular beams [100], and a recent textbook [101].

Although SIMS is not a traditional MeV-IBA technique, MeV heavy ions were used in the 1970s to sputter molecules from insulating materials in a technique known as PDMS [102]. PDMS instru-

ments were made using the fission fragments generated from a ^{252}Cf as a source of heavy ions, but it was found that a laser could effectively substitute for the radioactive source. The resulting technique, MALDI, has proved very successful, especially for biomolecules [103]. Recently it has been demonstrated that SIMS with an MeV primary ion beam can be used to generate molecular concentration maps on surfaces [104], this is the first use of "MeV-SIMS". Employing relatively light ions such as ^{16}O at 10 MeV it has also been shown that MeV-SIMS, RBS, and PIXE spectra can all be recorded simultaneously with the same primary ion beam [105].

Figure 18. Molecular Dynamics simulations showing volume of ejected and fragmented molecules after 10 keV fullerene impacts in solid benzene, and after the energy loss expected from 6 MeV O impacts into 10 benzene layers on a silver substrate.

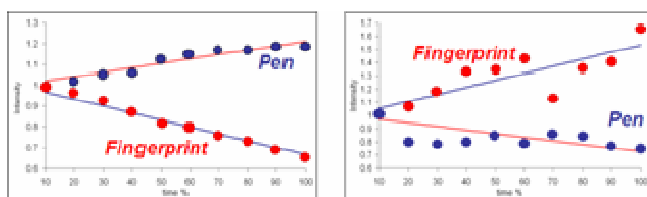


Recent work [106] has demonstrated that the damage cross-section of a sample of leucine (an essential amino acid) deposited on silicon caused by a 10 MeV $^{16}\text{O}^{4+}$ is comparable to that of conventional SIMS [107] using keV Ar^+ ions – $1.3 \times 10^{-14} \text{ cm}^2$. This is shown in Fig.17 where the logarithm of the leucine signal is plotted as a function of time. The signal decays as the molecular ion is fragmented by the primary ion beam.

The advantage of using low mass primary ions (eg. 6 MeV O) is that it is possible to also obtain simultaneous RBS and PIXE spectra and images with the same beam and hence at the same time (see Fig.5 of [105] for example). Experiments using higher mass primary ions (Cu) show substantially higher molecular yields and much lower fragmentation than has been achieved using low

energy cluster ions. The relative yield of a fragment peak (at $m/z = 147$ Da) to the principal peak (at $m/z = 1047$ Da) for an angiotensin II sample using a 6 MeV Cu^{4+} ion has been found to be up to 100 times that obtained using a 30 keV Bi_3^+ cluster (and 40,000 times greater than for 30 keV Bi^+) [108].

Figure 19. Depth profiles obtained from molecular fragment signals characteristic of fingerprint and ink. On the left the fingerprint is deposited over ink and on the right the ink is drawn over the print. That these cases can be distinguished has importance in forensics applications. Reproduced from Fig.4 of Bailey *et al.*, 2010 [110]

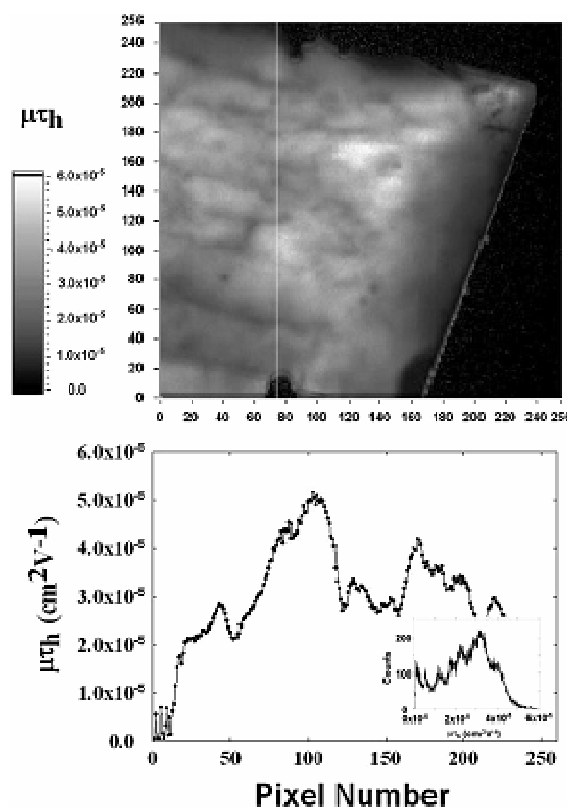


Simulation and modelling suggest that the process by which large molecular ions are ejected from the surface of molecular materials is similar for both MeV ion and keV cluster ion impacts (for the latter, see [109]). In Fig. 18 the volume of ejected and fragmented molecules is shown as predicted from Molecular Dynamics (MD) computer simulation for impacts on a frozen benzene (C_6H_6) target with keV cluster (C_{60}) and representative MeV ions. As can be seen, the ejection of material is from a conical region in both cases and the fragmentation occurs in a cylindrical region about the path of the impinging ion. The significant difference between the two results is that the length of the fragmentation cylinder is much longer for the MeV ions and the passage of the MeV ion causes substantial break-up of the molecular target over most of the pathlength of the ion. The path length of the keV cluster is relatively short, with the fragmentation cylinder also being short and barely extending below the ejection cone.

The implication of this is that depth profiling of molecular solids using keV cluster ions is feasible, with the possibility of maintaining reasonable signals from the principal sputtered molecular ion over large depths into the material. With MeV ions however, the molecular material will fragment at large depths and only lower mass fragments of the

target should be observable as the sputtering proceeds. This has been borne out in experimental work using this technique in which molecular images of doped fingerprints on paper over and under ink were analyzed [110]. Fig.19 shows the fragment signals of the molecular material representative of ink and fingerprint as they were followed to obtain depth profile information.

Figure 20. *Above:* Map of the hole mobility in $\text{Cd}_{0.9}\text{Zn}_{0.1}\text{Te}$ (with Au contacts) obtained from 2 MeV proton microbeam IBIC with spot size $2.5 \times 2.5 \mu\text{m}$. *Below:* Variation of hole mobility along the vertical white line in the map. Reproduced from Veale *et al.*, 2008 [115]



One of the great potentials of MeV-SIMS is that it can in principle be used in air, as MALDI is already. This is by no means simple but measurements have already been achieved at base pressures up to ~ 100 Pa (~ 1 mbar) [111]. The main difficulty is that of maintaining a high spatial resolution through air of such high mass ions; this means that the sample must be placed very close to the exit nozzle of the MeV-ion beamline, and then there is very little space left for the spectrometer.

3.5. *Electrical characterisation (IBIC)*

Ion beams striking a semiconductor will deposit electron-hole pairs all down the ion track. If these charge carriers experience an electric field then their subsequent drift results in a current and hence a signal on the device output terminals, similar to the operation of conventional semiconductor particle or photon detectors. In this case single ion impacts are detectable, and only very low beam currents are needed. In any case, higher beam currents would introduce noticeable damage into the detector! An application of IBIC (ion-beam-induced charge) was first reported in 1992 [112].

The ion beam induced charge (IBIC) in the detector is immediately visible as a mirrored charge on the device output terminals (the Shockley Ramo Theorem [113]), and monitoring the size and time evolution of the IBIC signal gives valuable information about the electrical quality of the device. The technique is typically used in microbeam imaging mode to investigate the spatial variations of charge transport properties, like the charge carrier lifetime and velocity, and to correlate those variations with other imaging techniques. Detailed analysis as a function of applied bias often enables the researcher to infer information about the internal electric field profile, hence also the space charge and details on carrier drift or diffusion (see [114] for an example involving angle resolved IBIC analysis of 4H-SiC Schottky diodes). When analyzing IBIC images, it is important to be aware that the volume that contributes to the formation of the signal is not limited to the range of the ion or its knock-on effects. On the contrary, the probed volume consists of all areas that the charge carriers drift through. Consequently the “spatial” resolution will vary with drift length and is often dominated by charge carrier diffusion rather than the ion beam diameter. Fig.20 shows the spatial variation of hole mobility in a high resistivity ($1.3 \cdot 10^{10} \Omega \cdot \text{cm}$) CZT device, obtained by mapping the charge collection efficiency as a function of bias voltage and then obtaining the mobility pixel-by-pixel from a Hecht analysis [115].

The corresponding electron mobility map for this device is very uniform, showing the uniformity of the electric field strength of the applied bias. Therefore, the non-uniformity of Fig.20 must be attributed to large scale variations of either drift mobility or carrier lifetime in the bulk material. Both of these can also be mapped, giving much detailed and valuable information about the type of crystal defects in the device as a function of position.

Due to the low beam currents used, IBIC can often be considered as non-destructive. Radiation damage can however affect the IBIC signal as damage typically induces additional electrically active defects that can modify both the carrier lifetime and mobility, and often also the space charge in the sample ([116]: in this case divacancy traps are produced by the beam).

During an IBIC experiment the charge carriers are generated deep (tens of microns underneath the sample surface) compared with the equivalent electron beam technique (EBIC) which only probes near the surface [117], just under the contact electrode and in some cases not even penetrating the electrode. In contrast, the deep interaction of the ion with the sample has even enabled researchers to probe buried structures in semiconductor devices (power devices [118] and MOS devices [119]). Typical EBIC experiments operate in continuous current mode (compared to pulse-by-pulse or ion-by-ion acquisition of the IBIC signals) and thus cannot analyse the transient current response to each interaction. But similar information to IBIC can be gained from XBIC experiments that are typically carried out with highly focussed monoenergetic X-ray beams available at synchrotron facilities (for example described for diamond devices in [120] [121]). The synchrotron source typically provides bunches of photons whose time structure and intensity depends on the source itself. If the bunch structure is short enough, similar time resolved information (lifetime and velocity profiles) can be gained as in an IBIC experiment (for CZT [122]). The X-ray energy range typically employed is in the order of tens of keV, which means that charge carriers are often generated

throughout more than a millimeter of the sample thickness. This often makes the experimental separation of electron and hole contributions to the signal impossible in thin samples, however X-ray induced charge carrier densities are lower compared to ion beam irradiation and therefore drift velocities extracted are less likely to be influenced by shielding of the effective fields due to the presence of the generated charge itself (subject to a sufficiently low X-ray flux). Both techniques require significant infrastructure and running costs and whether IBIC or XBIC is the method of choice will depend on the details of each individual study.

4. Particle-induced X-ray emission

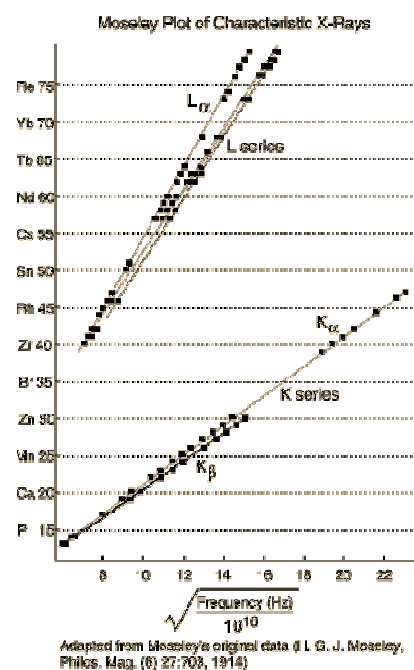
In a landmark pair of papers rapidly following Bohr's 1913 publication of his model of the atom, Henry Moseley investigated the characteristic X-rays produced when materials were bombarded with cathode rays (electrons). Since electrons are particles too, this is the first report of PIXE. In the first paper [123] he described the spectrometer (a crystal of potassium ferrocyanide), and pointed out that his "elemental" targets were contaminated with impurities saying, presciently: "The prevalence of [X-ray] lines due to impurities suggests that this may prove a powerful method of chemical analysis."

In his second paper [124] he systematically measured K- and L-series wavelengths (see Fig.21). The first report of α -PIXE was by Chadwick in 1914 [125]. But Charles Barkla is responsible for the first recognition of characteristic X-ray lines of elements, for which he received the 1917 Nobel Prize : it was in his 1911 paper that he first named X-ray "fluorescence", and introduced the "K" and "L" notation : mid-alphabet letters being used since both longer and shorter wavelengths were expected [126]!

The first report of modern PIXE using cooled Si(Li) detectors [127] was by Johansson *et al* in 1970 [128] who suggested that trace-element detection limits could be as low as ng/g, and analysed air pollution samples as an example. This rapidly led to a report of the variation of trace metal

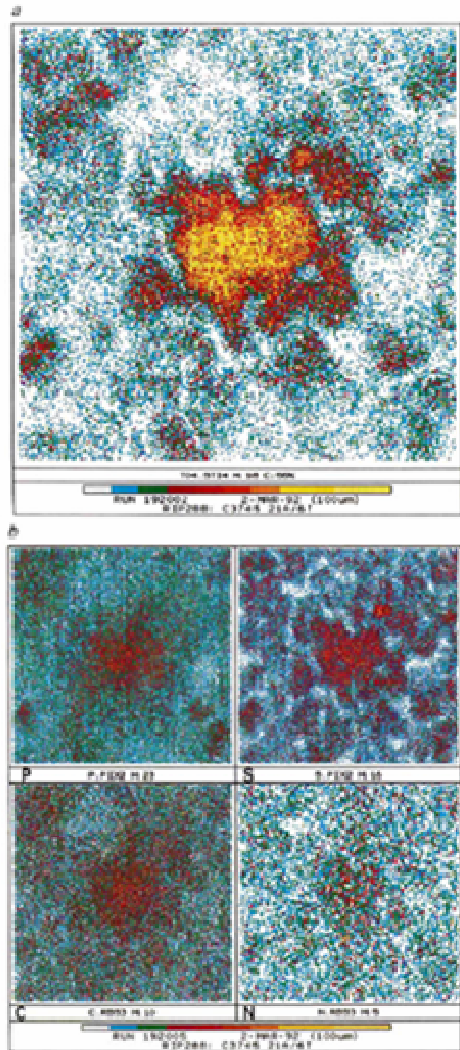
concentrations along single hairs [129]. Other highly cited examples using microbeam PIXE include measuring concentration gradients of pollutants in aqueous systems [130] and measuring the absence of Al in Alzheimer's disease samples [131] (see Fig.22).

Figure 21: Henry Moseley's measurement of characteristic X-ray energies. Adapted by R.Nave [132] from Fig.3 of Moseley (1914) [125]



Moseley used wavelength dispersive spectrometry (WDX) which is a high resolution technique quite capable of picking up differences in the electronic structure of the atoms due to different bonding states. This valence information is regularly used in EPMA, the electron spectroscopies (XPS, AES), and the absorption spectroscopies (EELS, XAS). It can also be used in PIXE if a high resolution detector is used, which could be WDX [133] [134], or one of the new high resolution calorimetric EDS detectors [135]. Of course, high resolution also allows disentangling of overlapping peaks which often occurs, especially for the L lines, and is one main cause of the degradation of sensitivity [136].

Figure 22. Scanning 3 MeV proton microbeam STIM, PIXE and EBS images ($100\ \mu\text{m} \times 100\ \mu\text{m}$) from sections of unstained *post-mortem* tissue of a patient suffering Alzheimer's disease. The spot size was $1\ \mu\text{m} \times 1\ \mu\text{m}$. **Above:** STIM map of region containing neuritic plaque; **Below:** Maps of the same area for P & S (PIXE), and C & N (EBS). Reproduced from Fig.2 of Landsberg *et al.*, 1992 [132]



Three physical effects have to be quantified to use PIXE for analysis: the ionisation cross-section, the fluorescence probability, and the mass absorption; these are all quite complex and need describing separately. To this needs to be added the energy loss of the incident particles in the sample, which is of course exactly the same as for the particle reaction techniques (see §2.1). We should note here that PIXE has its own ionisation physics, but shares the fluorescence (or, equivalently,

Auger) probabilities with the other atomic excitation methods (EPMA, XRF, XPS, AES, EELS, XAS). The X-ray absorption coefficients are also needed by the X-ray methods (EPMA, XRF, XAS).

4.1. Energy Loss (STIM)

We have noted in §2.1 that the ion beam will lose energy inelastically as it passes through the sample. If the sample is thin enough to allow transmission of the beam and a detector is placed behind it, then the average energy of the detected particles will be determined by the average sample thickness. If a microbeam is used, then an image of the sample density is projected onto the detector. This is the ion analogue of X-ray radiography.

Fig.22 shows STIM/PIXE/EBS maps of brain tissue in an important study which ruled out the presence of aluminium in brain tissue from Alzheimer's patients at levels greater than 15 mg/kg. The difficulty with previous studies is that the plaques characteristic of the disease are almost impossible to see optically without staining. But using STIM they can be easily visualised. Notice that in this case the contrast with STIM is very much larger (with orders of magnitude smaller beam fluence) than for PIXE.

STIM requires a very low beam current ($\ll \text{pA}$) since every particle is detected. On the one hand this means that the technique is the least destructive of any IBA technique, but on the other it means that the PIXE maps need orders of magnitude increase in the beam intensity. Therefore STIM and PIXE must be done sequentially. But PIXE/BS maps are collected simultaneously.

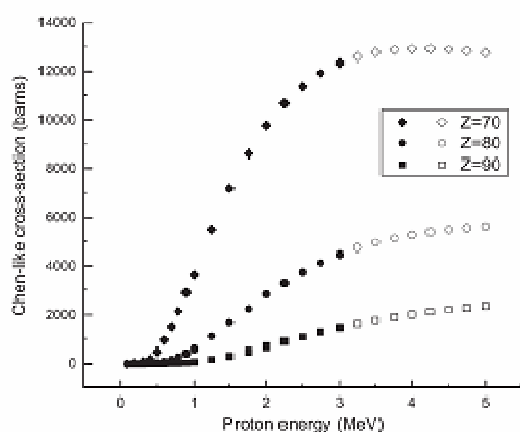
STIM/PIXE can be collected simultaneously if the detector is put off-axis so that it does not see the direct beam. This was first reported by Orlić *et al* in 1994 in a study of single aerosol particles [137].

4.2. Ionisation cross-section

Energetic particles implanted into a target will suffer inelastic energy loss as mentioned in §2.1. This energy is deposited mainly into the electrons of the sample. Thus, K-shell and L-shell (and

outer shell) electrons can be ejected from their shells, leaving the atom in an excited state. Semi-empirical models for the calculation of the probability of K-shell ionisation have been established by Helmut Paul and co-workers [138]. L-shell ionisation has been similarly determined by Miguel Reis and co-workers [139] with a polynomial representation for both K- and L-shells [140] and sub-shell ionisation cross-sections also extracted from the data [141]. Reliable data for M-shell ionisation is not currently available in the same form, but Fig.23 shows working values obtained by interpolation and extrapolation from ECPSSR^{XI} calculations (Campbell *et al* [142]).

Figure 23. M₁ sub-shell ionisation cross-sections for protons to 5 MeV. Reproduced from Fig.2 of Campbell *et al*, 2010 [142].



4.3. Fluorescence probability

The relaxation mechanism of the excited atom is complicated. But atomic spectroscopy has a very long history. The Doppler effect was first proposed by Christian Doppler as a means of detecting the motion of binary stars in 1842 [143], and observed (for sound, not light) by John Russell in 1844 [144]. Stellar spectroscopy was responsible for the discovery of helium in 1868 independently by both Janssen and Lockyer [145]. Bohr's model of the atom [146] was a triumph in 1913 precisely be-

cause it solved the problem of the hydrogen Balmer and Rydberg lines.

There are a variety of competing mechanisms. First is the possibility of a non-radiative transition by the Auger process. The branching probability of fluorescence instead of Auger relaxation has been calculated by Chen & Crasemann using ECPSSR theory for the K-shell [147], L-subshells [148] and M-subshells [149]. There are also extensive experimental data for the L-shell transition probabilities which have been critically reviewed by Campbell [150] [151].

The reason for this experimental interest in the L-shell fluorescence probability is that it is greatly complicated by the existence of the so-called Coster-Kronig (CK) transitions. These are a special class of nonradiative transition that transfers the vacancy from the initial subshell to a higher subshell within the same shell; that is, a re-arrangement of the electronic structure of the excited atom. The energy balance is preserved by the loss of outer shell electrons with appropriate energies; of course, quantum mechanical selection rules apply in all these electronic structure re-arrangements. There are very many CK transition probabilities to be determined, which can have a large effect on the relative X-ray intensities in the L, or M series; these intensities are therefore hard to determine, with large uncertainties remaining. Campbell and co-workers have given semi-empirical fitted data for the K [152] and L [153] series. Chen & Crasemann long ago calculated the relative line intensities for the M series [154]; this remains the best dataset available, since good experimental data for M-lines are hard to obtain. Therefore uncertainties for M-lines remain high.

In summary, the relaxation mechanism of the excited atom is far from simple. After the atom is ionised it can return to its ground state in a large number of different ways, many of which give X-rays at a variety of energies. This is a powerful probe of the atomic energy levels of the atom, but all of these effects must be understood reasonably well to use the fluorescence analytically. Recent work on L-lines using very high energy resolution EDS detectors has underlined the complexity of

^{XI} ECPSSR: Energy-loss Coulomb-repulsion perturbed-stationary-state relativistic theory

this process, and also the – potentially large – gaps in our understanding of it [155].

4.4. Mass absorption coefficient

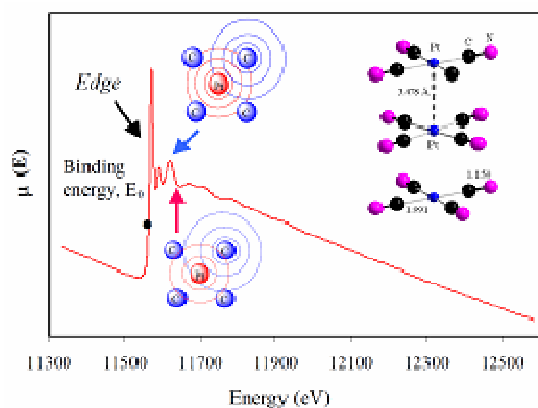
After the X-rays are produced in the interaction volume they still have to escape to the detector. Since the range of energetic light ions is large (>0.1 mm for 3 MeV protons in most materials) there may be a large thickness of material to absorb the X-rays before they reach the detector. Clearly, any quantitative work must take this into account.

The mass absorption coefficient (μ) is defined from the fraction of an X-ray beam (intensity I_0) that is absorbed during transmission through thickness x of a material. The transmitted beam intensity I is given by:

$$\ln(I_0/I) = \mu x \quad (6)$$

The XCOM mass absorption coefficient database from NIST includes comprehensive values for μ , and is kept up to date [156] [157].

Figure 24. X-ray absorption spectrum of Potassium tetracyanoplatinate $K_2[Pt(CN)_4]$ near the Pt L_{III} edge showing constructive and destructive interferences in the NEXAFS signal (figure drawn by Farideh Jalilehvand, University of Calgary, and reproduced from [158])



μ is a complicated function of X-ray energy. This is because absorption of the X-ray *suddenly* becomes possible as soon as the photon energy exceeds the binding energy of any particular atomic electron. Therefore there are absorption edges corresponding to all the atomic sub-shells. Actually, the situation is even more complicated than that since near the absorption edges there are

quantum mechanical interference effects, as shown in Fig.24.

Happily, these details are not usually important in PIXE, but the accuracy of the absorption database is of continuing concern in accurate work. Note that the absorption coefficient represents the sum of the cross-sections for three quantities: the photoelectric effect, and both of the incoherent and coherent scattering effects.

Work is continuing in the community to make further critical measurements of this (and other) important quantities. For example, the synchrotron group at the PTB, Berlin^{XII} recently used an absolutely calibrated instrument to make a determination of mass attenuation coefficients for Al [159] relative to previous values [160], finding internal inconsistencies in them of up to 10%. EXSA^{XIII} has promoted the "International initiative on x-ray (*sic*^{XIV}) fundamental parameters" which is coordinating efforts by all of the PIXE, XRF and EPMA communities to improve the various databases [161].

4.5. Quantitation and complementary methods^{XV}

It is important for analysts to appreciate that there are a number of other analytical techniques involving exactly the same atomic relaxation and X-ray absorption physics. The excitation methods are comparable, but have to be treated separately to give the detail required for analytical purposes. It is worth pointing out here that atomic ionisation with ion beams has complexities not present for the simpler photoionisation processes since higher charge states are much more probable.

Except that the excitation is via photo-ionisation instead of particle impact, the physics of the X-ray fluorescence (XRF) technique and PIXE are similar, with similar spectra, and detection limits only somewhat worse due to the presence of background

^{XII} PTB: Physikalisch-Technische Bundesanstalt, Germany's national metrology institute

^{XIII} EXSA: European X-ray Spectrometry Association

^{XIV} Properly, "X-ray" is capitalised, since the "X" is an abbreviation for the proper name Röntgen.

^{XV} This section is something of an acronym soup, for which apologies. Please see Appendix B for a Glossary.

radiation originating directly from the exciting beam. Desktop XRF instruments are in wide use, but these do not give monochromatic beams and calibrating the tube spectra is difficult. With synchrotron XRF a tunable monochromatic source is available, making this an exceptionally powerful analytical tool. However, at present mapping is still rather slow, and XRF spectra give no direct access to depth profiling.

A PIXE code should also be able to interpret XRF spectra, provided the photo-ionisation can be properly handled. Because the information depth for the two techniques is complementary there is sometimes an advantage in an XRF/PIXE analysis, as shown in recent work on Roman silver coins [162] and ancient glass beads [163]. On the other hand, the instrumentation of the Mars Rover has generated mixed XRF/PIXE data, the analysis of which is a *tour de force* that has established the presence of hydrated minerals on Mars, an extraordinarily important result [164]. Note that PIXE will always excite secondary fluorescence by XRF.

Electron-probe microbeam analysis (EPMA) is a scanning electron microscope (SEM) method specialised for X-ray analysis. Typically, an EPMA instrument will have both EDS and WDX detectors. Both EPMA and SEM-EDS (like XRF) have similar physics and observed spectra as PIXE: the only difference is that in this case the excitation is via electron impact rather than ion impact. But SEM methods have important analytical differences from PIXE. Electrons are 2000 times lighter than protons, and the primary Bremsstrahlung for protons is negligible. Therefore detection limits for SEM methods are orders of magnitude worse than for PIXE.

Also, because of the large lateral straggle for electron beams and for SEM energies (usually <30 keV) and thick targets, the excitation volume for electrons is determined by the electron energy and not by the probe diameter. But proton beams penetrate to large depths from which few X-rays escape. So the excitation volume for protons is determined essentially by the probe size. If ion microbeams can be built with sub-micron spot sizes (see §6.4), then PIXE maps will have better spatial resolution than SEM-EDS X-ray maps.

SEM-EDS and PIXE are similar in that for both techniques there is a backscattered particle available: for PIXE it is the BS signal, and modern SEMs usually have a BSE detector for Z-contrast. But the SEM-BSE signal cannot be treated quantitatively without great difficulty (Monte-Carlo methods are needed), and therefore, as with XRF, any depth profile is not accessible directly with SEM methods.

EDS detectors are also often installed on TEM instruments. In this case the samples are always thin, but their absolute thickness is usually hard to obtain and so the X-ray spectra are rarely treated quantitatively. However, modern TEM instruments often also have an EELS attachment. This is the *inverse* process to AES: in EELS the effect of the atomic structure (including chemical effects) on the transmitted electron energy is observed.

The electron spectroscopies (XPS and AES) excite the atom with photons and electrons respectively, energy-analysing the electrons resulting from atomic relaxation. XPS is a one-electron process with the photoelectron observed directly. AES is a process involving at least three electrons, which occurs when the atom relaxes non-radiatively. Of course, Auger electrons are also observed in XPS spectra. Because the energy resolution available is high (<1 eV) chemical effects are easy to observe.

The X-ray absorption spectroscopies should also be mentioned (see Fig.24 and an example on nickel oxy-compounds [165]). These include XANES, EXAFS and NEXAFS as synchrotron techniques, and are analogous to EELS in the same way that XRF (X-rays in, X-rays out) is analogous to AES (electrons in, electrons out).

These techniques with others are frequently used in conjunction. For example, a recent review of methods to visualise spatial distributions and assess the speciation of metals and metalloids in plants addressed: histochemical analysis, autoradiography, LA-ICP-MS^{xvi}, SIMS, SEM-EDX, PIXE, XRF, XAS, and differential and fluorescence tomography [166].

^{xvi} Laser ablation ICP-MS

4.6. Depth profiling with PIXE

PIXE spectra (like EPMA or XRF spectra) do not give information about possible depth profiles directly, although of course the line intensities are greatly modified by how much they are absorbed on their path to the detector; also, because the ionisation cross-sections are a strong function of energy, the number of X-rays produced is a strong function of depth. To access this information, the profiles must be inverted from the spectra, and this problem is in general mathematically ill-posed.

If the sample structure is known *a priori*, then the structure parameters (layer thicknesses etc) can be modelled from the data. This is routine for XRF, for which software is commercially available. But if the sample structure is not known then single PIXE (or XRF or EPMA) spectra are almost always ambiguous.

XPS has exactly the same problem, and with the same solution. Angle-resolved XPS has received careful attention [167], and differential PIXE can vary either the beam energy or the angle of incidence: we mention recent work on multi-layer targets [168] and a recent review of cultural heritage applications [169].

5. IBA codes

The brief sketch we have given so far of the physics of the MeV-IBA methods used for depth profiling makes it very clear that computer codes are needed to make any systematic use of these methods for analytical purposes. In this section we will make general and technical remarks about the codes specifically for photon emission and particle reactions, and in §6 we will concentrate on integrating these methods.

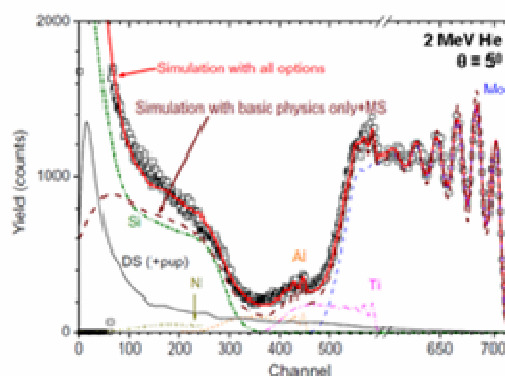
We will consider stopping power and straggling effects (roughness, variable density, phase separation) in §5.3 since in principle these affect both the particle and the photon techniques

We will not consider non-depth-profiling techniques (channelling, MEIS, IBIC); nor will we cover the low energy or sputtering techniques (LEIS, MEIS, SIMS). For further details see §3.

5.1. Codes for nuclear reactions

Codes for (mostly) depth profiling using particle scattering and non-resonant nuclear reactions were reviewed in IAEA-sponsored work by Rauhala *et al* in 2006 [170]. A detailed Intercomparison also sponsored by the IAEA of selected codes was subsequently completed [171], with a brief Summary also available [172]. The Intercomparison identified two "new generation" advanced codes (**SIMNRA** [173] [174] [175] and **DataFurnace**^{XVII} [176] [177] [178]) that performed excellently and had all the facilities needed to treat the complex cases we will discuss below. SIMNRA and DataFurnace are analytical codes based on the single scattering approximation, with other effects introduced as perturbations. In most cases they give indistinguishable results, but DataFurnace is specifically aimed at handling multiple spectra self-consistently where SIMNRA is designed only for single spectra.

Figure 25. High resolution (glancing incidence) analysis of a tribological coating: TiAlN / Mo multilayer on Si, modulation period 3.9 nm [179] (reproduced from Fig.1 of Barradas & Jeynes, 2008 [177]). Simulations are shown : including only symmetrical effects due to multiple scattering; showing the double scattering and pileup background; the full simulation including the low energy yield (partial spectra for Ti, Al, Si, N also shown for this case)



Both SIMNRA and DataFurnace allow fitting of RBS, EBS, ERD, and (non-resonant) NRA spectra to models using standard algorithms (Simplex for SIMNRA and grid-search for DataFurnace [180]).

^{XVII} DataFurnace is also known as NDF.

DataFurnace also allows model-free fitting with the simulated annealing algorithm [181], which facilitates the natural implementation of a Bayesian algorithm for the reliable estimation of the uncertainty of the resulting depth profile [182].

Both SIMNRA and DataFurnace use the accurate pulse pileup algorithm of Wielopolsky & Gardner (1976) [183], and DataFurnace also implements both triple pileup [184] and Molodtsov & Gurbich's more accurate calculation [185]. DataFurnace also implements Lennard's [186] pulse height defect algorithm [187].

Both SIMNRA [188] and DataFurnace [189] can calculate the effect of roughness on backscattering spectra; SIMNRA is aimed at gross roughness such as is found on tokamak facing tiles, where DataFurnace is aimed at fine interface roughness effects such as is found in magnetic superlattice samples. But neither can correctly model really severe roughness such that the beam enters (or exits) the sample multiple times (through asperities). Molodtsov *et al* [190] implement a general algorithm which will allow the effects of such severe roughness to be interpreted, but this algorithm is not yet implemented in any general purpose IBA code. SIMNRA allows calculation of the effect on spectra of roughness whose model parameters are known (perhaps from AFM measurements), using a spectral^{xviii} summing method (see [191] for a recent example). DataFurnace allows fitting of given spectra, from the parameters of simple models for the roughness of interfaces or layer thickness inhomogeneity; sub-*nm* sensitivity was demonstrated for magnetic multilayers [192].

The algorithm of Stoquert & Szörenyi [193] allows the calculation of the effect of precipitates (density variation) on the spectra. DataFurnace [48] implements this algorithm and SIMNRA [194], implements a more accurate comparable algorithm. On the other hand, DataFurnace implements EBS resonances more correctly than SIMNRA (see Fig.6 and [47], and see the Intercomparison [171]

for more detail). The difference is noticeable for sharp resonances. DataFurnace also implements a good approximation for low energies [195] (see Fig.25).

Finally, both SIMNRA [174] and DataFurnace [196] implement similar algorithms for double scattering. The symmetrical components of multiple scattering are handled with Szilágyi's algorithm [197] [198] by both codes. DataFurnace uses DEPTH [199] directly, and SIMNRA implements the algorithms (see the discussion in [200]). Kinematical broadening and related effects are also treated. These effects become large for glancing incidence geometries, such as are used for high resolution or ERD. See Fig.25 for an example showing all these effects.

For high depth resolution RBS, and for ERD especially HI-ERD, glancing incidence beams are typical. In these circumstances multiple scattering and related spectral distortion effects become important, and the uncertainty of the analytical codes' calculations increases. **CORTEO** [201] [202] is a Monte Carlo code designed for routine use, optimised for speed and entirely comparable to the code MCERD [203] described in the Intercomparison. It also enables the detailed simulation of geometrical effects, including the geometry of the detector (typically ToF for ERD).

For high resolution resonant NRA, sharp resonances (usually at low energies) are used to probe depth profiles. In these circumstances the approximations normally used for straggling fail close to the surface, where the fundamentally stochastic nature of the straggling cannot be approximated by a continuous (Gaussian) distribution. The **SPACES** code [204] [205] takes this into account. DataFurnace has been extended to treat resonant NRA, and by using a gamma function approximation to the straggling (as SIMNRA does for roughness) also treats high resolution NRA [206], giving results comparable to SPACES provided the Lewis effect [207] is not too large.

^{xviii} The noun is *spectrum*; the adjective is *spectral*. From Newton's usage (p.1) and the Latin, *specere*, to see.

5.2. Codes for atomic excitation

The first full account in 1989 of the **GUPIX**^{XIX} code [208] starts very helpfully for those wishing to appreciate what is involved in PIXE (or XRF, or EPMA) spectral analysis:

"The typical PIXE or micro-PIXE arrangement employs a Si(Li)^{XX} detector to record the spectrum induced in an analytical specimen by [typically] 2-4 MeV protons. Elements of low and medium atomic number each contribute about six distinct K X-ray lines and those of high Z each contribute about twenty L X-ray lines. The lines, approximately Gaussian in shape, are superimposed on a continuous background arising from various bremsstrahlung [*sic*^{XXI}] processes [comprehensively described by Ishii & Morita, 1984 [209]] and sometimes also from nuclear reaction gamma rays. The resulting Si(Li) spectrum is complex and peak overlaps occur frequently."

GUPIX itself dates from 1984, and codes then available (including Clayton's PIXAN) were reviewed and compared in 1986 to evaluate PIXE as an analytical technique [210]. Campbell *et al* go on to describe the way GUPIX handles the particle impact ionisation, the fluorescence probability and the absorption calculation databases. They consider the non-Gaussian Si(Li) lineshapes, the method for stripping the Bremsstrahlung background from the spectra, and the details of the complex fitting procedure used. Subsequent work implemented secondary fluorescence, and later versions of GUPIX (see citations in the 2010 paper [142]) have continued to refine this program.

Currently, GUPIX does not permit the calculation of PIXE spectra from general multilayer samples: multilayered samples are only supported provided that elements of interest appear in only one layer. This is an arbitrary restriction that will

^{XIX} The "Guelph PIXE software package"

^{XX} Si(Li): lithium drifted silicon diode detector (pronounced "silly"). These are typically up to 5 mm thick, giving good absorption of X-rays below about 30 keV energy. It is hard to make such thick crystals without recombination sites in the electrically active region (destroying the linearity of the device) and the defects are passivated by a lithium drift process. There is a similar process for Ge(Li) ("jelly") detectors, but these have now been superseded by high purity (HPGe) crystals.

^{XXI} As a German noun, "Bremsstrahlung" is properly capitalised.

be lifted in future versions. The distributed version of GUPIX also does not support XRF spectra, although there is a version that does which was used for analysing the Mars Rover data [211] [212].

GeoPIXE [213] was first described in 1990 [214]. Unlike GUPIX, GeoPIXE is explicitly for microbeam applications, and includes true-elemental visualisation; in 1995 a version was described able to correct in a very elegant way for differential self-absorption in samples with different phases (very common in geological applications) [215]. GeoPIXE is still being actively developed, now supporting large detectors and high count rates [216], and STIM [217]. We should note that GeoPIXE also supports XRF spectra.

Axil^{XXII} was originally a commercial XRF program from Canberra-Packard [218], was rebuilt in 1994 [219], and explicitly applied to PIXE in 1996 [220]. It is now publicly available from the IAEA XRF Laboratory [221] and commercially (with a windows GUI) from Canberra [222]. Both versions are aimed at energy dispersive XRF applications.

OMDAQ^{XXIII} was first reported in 1995 [223]. This code was the first to make a systematic use of the particle BS spectrum to give a reliable charge normalisation and the sample thickness measurement essential to doing the X-ray absorption correction, and is specifically aimed at microbeam applications. For handling the PIXE spectrum OMDAQ relies on the GUPIX code.

Where OMDAQ is a microbeam PIXE code that makes (quite simple) use of the particle spectrum, **DataFurnace** is originally a nuclear code (RBS/EBS/ERD/NRA) extended to accept PIXE data and designed to handle atomic and nuclear data self-consistently at the highest accuracy possible [224]. It relies on calling the open-source PIXE module **LibCPIXE** (2006) [225] which implements the 1996 **DATTPIXE**^{XXIV} code by Miguel

^{XXII} Axil: Analysis of X-ray spectra by Iterative Least squares fitting. Of course, GUPIX also used iterative least squares fitting, but was ignored by the XRF people since it was a PIXE code!

^{XXIII} OMDAQ: Oxford Microbeams data acquisition

^{XXIV} TTPIXE: thick target PIXE, first published in 1992

Reis and co-authors [226]. As PIXE input, DataFurnace currently takes line areas obtained by preprocessing raw PIXE spectra using AXIL or GUPIX. At present, DataFurnace has not implemented the secondary fluorescence correction. Developments which will be applied in future to the DataFurnace PIXE module are continuing under the pressure of difficult high resolution spectra from an EDS detector based on a micro-calorimeter. It is important to be able to handle raw spectra [227], since the recognition of the lines, and the determination of line ratios, cannot be done either by AXIL or GUPIX in a model-free way.

Finally, we should mention that **GEANT4** has now also implemented a PIXE module [228].

A fundamental limit to the accuracy of PIXE is down to the uncertainties in the various databases used, as highlighted by the Fundamental Parameters Initiative of EXSA [161]. The discussion here has shown that the calculations are extensive and rather complicated, and a "fundamental parameters" approach is not likely to yield uncertainties much smaller than 20%, except in particular cases where values have been specially determined (see [159] as an example).

Where better accuracy is required the usual procedure in the PIXE/XRF community is to calibrate the fundamental parameters used against standards: of course, relative accuracies <1% are easily obtainable in simple cases; even for complex samples, accuracies ~5% can usually be demonstrated with appropriate standards.

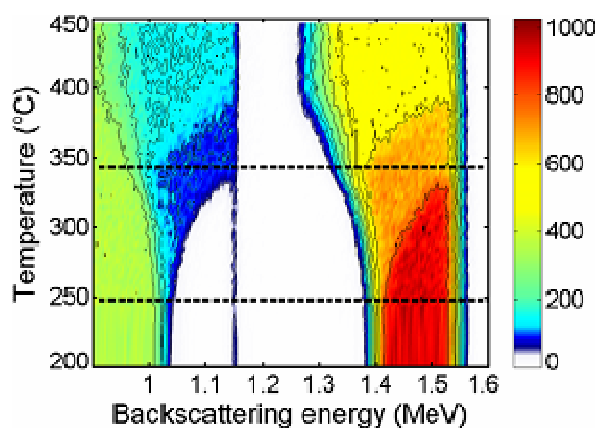
The accuracy of the PIXE codes themselves has been confirmed in an IAEA-sponsored Intercomparison exercise [229] [230]. Subsequently, LibCPIXE and GUPIX (and SEM-EDS) calculations have been critically compared (for hydroxyapatite) [231].

5.3. Artificial neural networks

There is a new approach to IBA which may prove remarkably valuable. Artificial neural networks (ANNs) can be constructed capable of effectively analysing various classes of IBA data [232].

O'Connor & co-workers discuss this "inverse problem" with noisy data, and directly compare ANNs and simulated annealing [233]. Fig.26 shows real-time data obtained to determine the detailed annealing kinetics of the nickel silicide system [234]. This is a simple example: there are a number of other examples not so simple. Much intervening work has shown that ANNs can be trained to handle multiple spectra, or multiple techniques; and it is clear that any sort of IBA can be implemented in an ANN for which a valid training set can be defined (although an ANN system for PIXE has not yet been reported).

Figure 26. Composite of 250 RBS spectra taken during a Ni silicidation reaction of an 80nm Ni film on silicon, capped with 7 nm of Si and annealed at 2°C/min. The colour code on the right shows spectral intensity in arbitrary units. The dashed lines indicate the initiation of the mono- and disilicides. (Reproduced from Fig.2 of Demeulemeester *et al.*, 2010 [233])



The point here is that once the ANN has been trained, a solution of a spectrum is obtained completely automatically and effectively instantaneously. This solution is itself remarkably accurate and, provided the ANN training is adequate, will be qualitatively correct. Such a solution can be given back to the analytical codes for post-processing to automatically obtain the best possible solution, together with robust estimates of the uncertainty. Thus, the qualitative recognition of a set of spectra by an ANN can be used as the basis of an automatic and fully quantitative machine analysis of the dataset. To check whether individ-

ual spectra are actually validly analysed by the ANN (based on the sampling space of its training set), prior to passing them to it, an additional ANN can be trained that classifies spectra as "acceptable" or "not acceptable" (see [234]). Thus, the ANN can not only recognise a given spectrum, but can also recognise whether or not it has been trained to recognise it.

The aim is a push-button (or turnkey) system suitable for non-experts ("*IBA without Humans*"! [235]), similar to the systems already available for SEM-EDS, or EPMA or XRF, or even AMS. Such IBA systems would be essential for a more general industrial acceptance of the technique, and seem to be feasible.

5.4. *Accurate IBA*

It is extraordinary that the idea of an Uncertainty Budget [236] to quantify experimental and traceability uncertainties for IBA was only recently published by a National Metrology Institute (NMI) [237]. However, no NMI now has IBA capability despite their previous interest in the use of RBS in particular for metrology (NPL for a Ta₂O₅ standard material [238] and a metrology exercise on the native oxide of Si [239]; IRMM and BAM for the certified reference materials used for fluence standards in IBA (the "old Harwell" Bi-implanted standard [240] and the new Sb-implanted certified reference material ERM-EG001 from IRMM/BAM [241])^{xxv}. The situation incidentally is entirely different for XRF, for which the PTB has been active in obtaining ISO 17025 certification and where the "Fundamental Parameters Initiative" is supported by no less than three National Standards Institutes (PTB, LNE, NIST [161]). Of course, this FP initiative has as much relevance to PIXE as it has to XRF.

^{xxv} NPL, IRMM, BAM, PTB, LNE, NIST: *National Physical Laboratory* in London, *Institute for Reference Materials & Measurement* in Geel, *Bundesanstalt für Materialforschung und –prüfung* and the *Physikalisch-Technische Bundesanstalt* in Berlin, *Laboratoire national de métrologie et d'essais* in Paris, *National Institute for Science & Technology* in Gaithersburg.

The qualification of implantation fluence is valuable for many different purposes, and is the simplest of RBS problems. We have already demonstrated an absolute accuracy of about 4% (95% confidence) in its determination [242] [243] [244], where the cited uncertainty was dominated by the uncertainty in the stopping powers used. However, we have demonstrated that for 1.5 MeV He in Si, the SRIM2003 stopping powers are accurate at 0.8% (1 σ , see Fig.1 in [172], but note that there are extra unaccounted uncertainties here [245]), and therefore the absolute traceable accuracy of RBS should approach 1% (1 σ) if this beam is used with a-Si substrates to determine the actual charge.solid-angle product for a given spectrum. RBS with 1% accuracy is rather hard to achieve: 1% accuracy has often been claimed (the report by Turkovich *et al* on the analysis of moon rocks by Surveyor V in 1967 is an important early example [246]), but there has been only one such previous *critical* report [247], and that was the rather special case of the RBS determination of the In:Ga ratio in InGaAs samples. There is no other thin film technique that can match this level of absolute accuracy for the determination of quantity of material. To achieve this accuracy it is necessary to correct properly for pulse pile-up, and to correctly determine the electronic gain of the detectors, including the appropriate pulse height defect correction (see §5.1).

For any sort of accurate IBA, an essential prerequisite is the availability of statistically robust estimates of the uncertainty of the result. Such an estimate is entirely absent in the classical approach to solving RBS spectra where manual simulations are made until a plausible fit is obtained. Such an approach (discussed at length in [176]) is not even adequate to explore the intrinsic ambiguity of the data! A fully Bayesian (maximum entropy) approach to this has been made [248] but has not proved to be generally usable. Although astonishingly good results can be achieved, the calculations are very time consuming and the information needed about the system is prohibitively detailed. However, a cruder approach using the DataFurnace code, still Bayesian but not using maximum

entropy, has proved to be of general use in IBA depth profiling.

This approach was used for the example shown in Fig.1: hence the extraordinary precision for the layer thicknesses obtained in this multilayer sample. Note that one of the virtues of this approach is that it allows the systematic evaluation of explicitly stated prior assumptions imposed on the data. In this case sub-nm precision in the layer thickness determination, even at the bottom of the stack, is obtained *assuming* that the sample has alternating layers of zirconia and silica. Then the precision represents the precision with which the signal areas can be obtained, *given the structure*. Analysts using informal fitting methods invariably have assumptions they impose on the data: unfortunately, too often these assumptions are hidden, and the analyst is unaware of them.

It is worth emphasising that this approach to uncertainty in the DataFurnace code is quite general. It is applied to all the data submitted for self-consistent analysis, currently including PIXE, RBS, EBS, ERD, PIGE, NRA and NDP (neutron depth profiling, see [249] for an example of this technique).

We should point out that for a valid estimate of the total combined uncertainty, an estimate of the database uncertainty is also required. The stopping powers used are usually from a semi-empirical compilation whose uncertainty in any particular case can generally be estimated quite well. But in cases where the stopping power is not known, or not known well enough, a Bayesian method of extracting the stopping power from thick sample spectra [250] is particularly valuable, since it also gives the uncertainty. EBS cross-sections on the other hand should properly be obtained using thin film samples, although some evaluations also make use of thick film data inverted to obtain the cross-section (see [251] [252] as examples). But evaluations of EBS cross-sections (see [44]) do not as yet include any reliable estimate of the uncertainty since these are very complicated to calculate correctly. Even the RBS/EBS boundary is not known with precision (see Table 1). Clearly this is a major problem for accurate (traceable) analysis that needs evaluated

EBS cross-sections. We believe that one useful approach to determining such uncertainties could include uncertainties obtained from benchmark measurements which use this Bayesian method [253]. But this approach is still to be properly developed.

6. "Total IBA"

We now put together all the ideas presented so far, and consider the benefits of combining IBA techniques to increase their power.

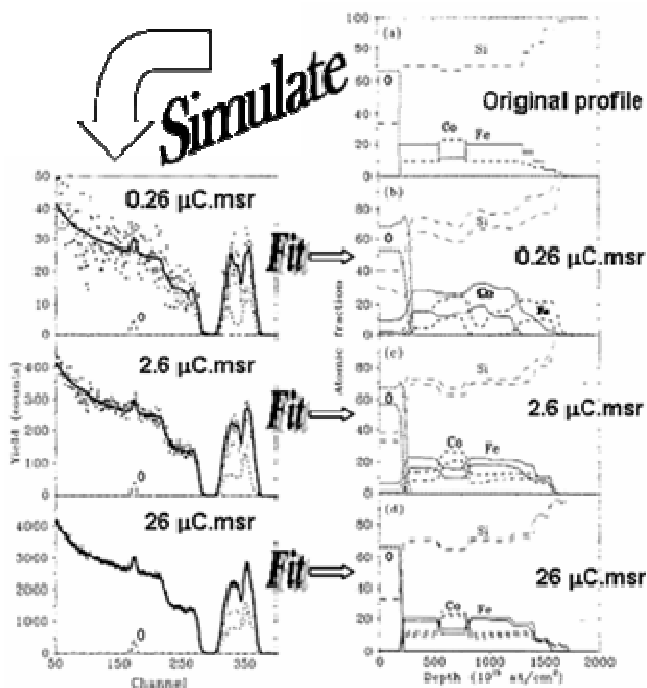
Our thesis here is that the old approach of IBA labs, where RBS was mainly on offer in one lab and PIXE mainly in another, is not sustainable in the second decade of the 21st century. RBS is good for heavy elements in a light matrix and typically the mass resolution is not very good, so that only fairly simple things can be said about fairly simple samples. On the other hand, PIXE cannot compete on price against the almost equivalent XRF (there is even an explicit comparison of PIXE with XRF showing their near-equivalence [254]), and for half the price of microbeam PIXE equipment would you not be better off investing in a micro-XRF? Why bother with IBA at all?

But we believe that if an integrated approach is taken, where multiple detectors are used with every analysis beam so that some combination of PIXE / RBS / EBS / ERD / PIGE / NRA is always systematically done, then not only does the range of samples for which IBA is appropriate increase dramatically but also the quality of information about each sample also increases. We will mention several cases where neither the backscattered particle signal nor the emitted photon signal by themselves could solve the sample; but where the solution is straightforward when multiple signals are treated self-consistently.

Why have the laboratories using PIXE and backscattering (BS) historically been so separate? There are good and bad reasons for this. Undeniably, for samples where the trace element content is important, BS often adds little useful information; similarly for PIXE where a layer thickness is required. Also, PIXE quantification is rather

troublesome, with quite a long traceability chain; so that if accuracy is required for the major elements seen by BS, then PIXE adds no information.

Figure 27. Noisy spectra can contain crucial information! 1.5 MeV He RBS spectra of a mixed Fe:Co silicide on a Si substrate are simulated from an initial structure (*top right*), given various charge.solid-angle products (*left hand column*). These simulated spectra are treated as data, fitted (lines), and hence inverted back to depth profiles, with uncertainties given by a Bayesian analysis (*right hand column*). Modified from Figs.1&2 of Barradas *et al*, 2000 [182]



Moreover, because the cross-section for PIXE is large relative to RBS, microbeam maps obtained from the particle detector have a very low number of counts compared to those obtained from the X-ray detector. Do very noisy spectra have negligible information? This is emphatically denied by a Bayesian analysis [182] of the complicated 3-layer mixed Co:Fe silicide shown in Fig.27! The qualitative structure could easily be resolved from the RBS spectrum with a very small charge solid-angle product of only 0.3 $\mu\text{C.msr}$ (readily obtained in $\mu\text{beam-PIXE}$). It is very clear that it is completely *false* to assume that the noisy BS spectra obtained in regular $\mu\text{beam-PIXE}$ mapping are effectively information-free: on the contrary, these

spectra frequently contain crucial information. For example, in such mixed silicides the absorption of the metal K lines even in relatively thin layers will be significantly different for different layer structures. This conclusion is underlined by recent work that shows that robust information is available even in the presence of 10% Poisson noise [232].

For PIXE a very common beam to use is 3 MeV H^+ . This is because the production cross-section goes up with beam energy, but beyond this energy nuclear reaction products tend to also decrease the signal to noise ratio. Thus this beam usually gives about the best available sensitivity. However, for this beam the particle scattering is non-Rutherford up to at least Fe (see Table 1). In the last ten years the (non-Rutherford) differential scattering cross-sections for most of these reactions have been measured and evaluated, so that today we can usually do analyses with an accuracy previously unthinkable, and even at sharp resonances. So although in the quite recent past it was reasonable to discount the particle spectra on the grounds that they were uninterpretable, today this would be a grave mistake.

Therefore, although even in the quite recent past it was understandable that self-consistent PIXE/BS was often judged to be too problematical to be worth the effort, this is not the case today. We should point out that self-consistent PIXE/BS has been available for a long time (OMDAQ [255] and "IBAlab" [256]), and accurate analysis using "Total IBA" has been applied recently to applications in geochemistry (PIXE/BS/ERD, [257]), biomedical surfaces (PIXE/BS, [258]), Alzheimer's disease (mapping STIM/PIXE/BS, [259]), amino-functionalised gate oxides (RBS/ERD, [260]), fish otolith composition (microbeam BS/ERD/PIXE, [261]), cultural heritage studies in the Louvre Museum (BS/PIXE, [262]), and multilayer materials (RBS/EBS/PIXE/HR-PIXE, [263]): in the latter case high energy resolution PIXE was also essential.

6.1. Nuclear and atomic methods compared

We believe that great synergistic advantage results when photon and particle spectra are analysed self-consistently. Where BS spectra typically have

rather poor mass resolution, PIXE spectra usually have excellent mass discrimination. Conversely, where depth information is implicit in PIXE spectra, it is explicit in BS spectra.

There are two important ways where the various IBA methods do not match well. Roughly speaking, PIXE X-ray production cross-sections are typically of the order of thousands of barns, RBS scattering cross-sections of the order of barns and NRA reaction cross-sections of the order of milli-barns. Clearly trace element analysis using NRA with microbeams is not usually going to work very well. And handling the noisy BS spectra that are common in μ PIXE work has its own pitfalls. Nevertheless, we here show many cases that powerfully demonstrate that important results are available despite this mismatch in signal size.

Just to emphasise that this mismatch between PIXE and PIGE is not limiting, there are *hundreds* of papers using both techniques, from the Namur group on ancient gold jewelry in 1982 [264] to the Florentine group on atmospheric aerosols in 2010 [265], and of course the reason for this is precisely that PIXE runs out of sensitivity for the light atoms (F, Na, Mg, Al) for which there are good PIGE reactions and which are of crucial importance in many materials.

The second mismatch is in information depth. Roughly speaking, the information depth for PIXE is around 20 μm or so (more or less depending on the X-ray line), for RBS it is 10 μm or so (for a proton beam, some five times less for a He beam), this is because the scattered particle may not have the energy to reach the detector from deep in the sample. For NRA it depends on the reaction. But PIGE is very sensitive to the light elements, and γ -rays are excited (for non-resonant reactions) along most of the length of the ion track. γ -rays are not absorbed readily and in most cases it is a reasonable approximation to assume no absorption on the pathlength to the detector. So, although for BS/PIXE the analyst must beware that the PIXE spectrum is giving information for a much thicker layer than for the BS spectrum, for PIGE/PIXE this mismatch can be a positive advantage. For the important element Na for example, the PIXE spectrum information depth is very small where that for PIGE is very large: the

PIGE/PIXE combination then gives differential information about surface Na loss which is rather hard to obtain otherwise. This is one of the essential points made by both the PIXE/PIGE papers cited.

6.2. Nuclear and atomic methods combined

The examples already mentioned of multiple IBA techniques used together mostly handle the individual spectra individually. We will here give a number of examples of "*Total IBA*" showing the extra analytical power available where multiple spectra can be handled together self-consistently.

Protein crystallography is an important example where IBA is used to interpret another technique: in this case the bound metal ions or co-factors cannot be uniquely determined by X-ray or NMR methods. PIXE has the sensitivity to detect the metals, which are usually in trace concentrations, and uncertainty is avoided by the use of the intrinsic protein S content as an internal standard for normalisation. The critical feature of this method, on which its accuracy depends, is the use of the BS spectrum by the OMDAQ code for an internally consistent X-ray absorption correction [266] (and see [267] for a recent example on a variety of *E-coli*).

The DataFurnace code was used to analyse Niepce's heliograph of 1827 [268], a 19th century reproduction of Frans Hals' *La Bohémienne* [269], oxidation of carbon nanotubes [270], and photovoltaic and ferroelectric materials [271] [272] [273]. The *La Bohémienne* analysis followed a PIXE/BS analysis which was not self-consistent [274], but was itself flawed by an incorrect treatment of the sample roughness. Using a correct analysis of this same data, Molodtsov *et al* [190] have shown that gross surface roughness can be treated correctly; moreover, IBA can be used in principle with good sensitivity to determine the average roughness parameters of a sample without any prior model and also without any surface contact!

A number of different forensics applications are being developed at present (see a recent collection of papers [275]): in principle the analysis of sam-

ples for forensic purposes should be fully quantitative and non-destructive. The previous discussion makes it clear that IBA can be accurate even for complex samples requiring the use of multiple IBA techniques. Gunshot residue (GSR) analysis by IBA looks very promising: interestingly, current police practice uses exclusively qualitative SEM-EDS as a characterisation technique. Different GSR particles which can be recovered from the crime scene and from suspects can be shown to distinguish the primers for the explosive charge used by different gun manufacturers. Electron-induced PIXE has no explicit depth information, and poor sensitivity because of the high primary electron Bremsstrahlung background. SEM-EDS therefore cannot discriminate many modern primers, limiting its usefulness for forensic evidence. We have shown that PIXE/BS can give very sensitive *quantitative* information on many types of primer [276] [277] thereby giving IBA substantially increased discrimination power over SEM-EDS.

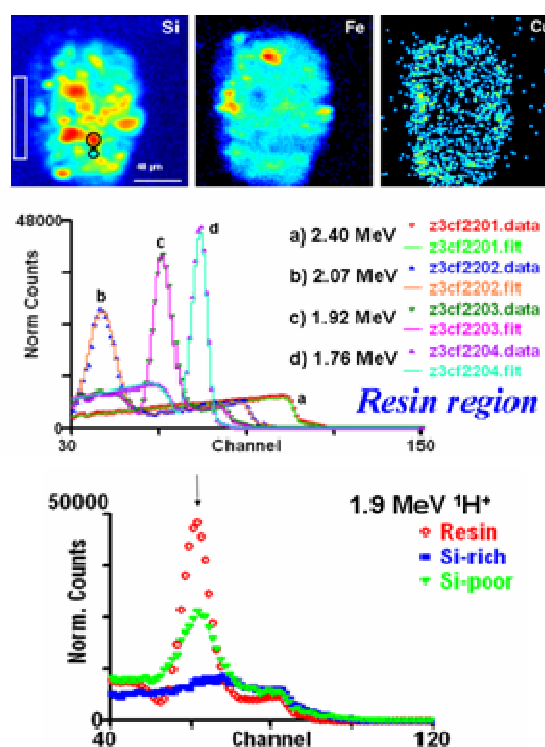
6.3. 3D PIXE/BS, the Darwin Glass example

Another interesting example is of the so-called Darwin glasses [278] which are impact glasses resulting from a meteor strike 800,000 years ago near Mt. Darwin in Tasmania. The geologist who collected these glass samples subsequently used one of them as an amorphous standard for setting up his XRD kit, and was astonished to see the diffraction spots of quartz. These crystals – unexpected in a glass! – turned out to be inside *inclusions* in the glass.

But the nature of these inclusions was then entirely unknown to the geologists. IBA analysis unequivocally demonstrated them to be carbonaceous, a result that initially baffled the geologists, for whom such a sample was unprecedented. Moreover, not only did the microbeam PIXE/BS determine the main constituents and demonstrate the great heterogeneity of the samples (both laterally and in depth: see Fig.28, and Fig.1 of [279], for example), but the IBA data could be com-

pletely quantitatively analysed without any presupposed model despite the heterogeneity.

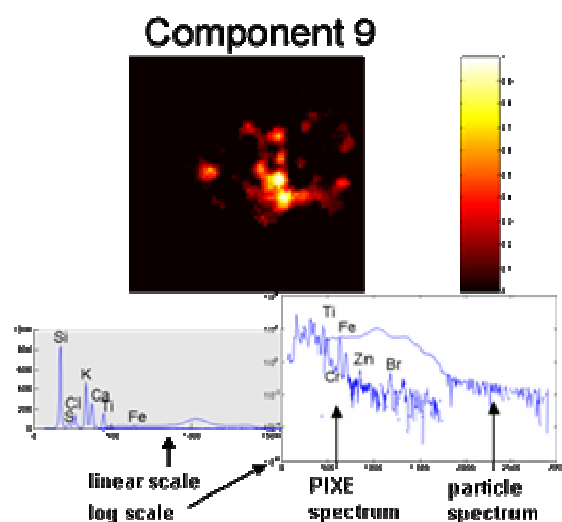
Figure 28. "Total IBA" of an inclusion in a Darwin Glass (see text). *Above:* selected PIXE maps showing distribution of Si, Fe, Cu; *Centre:* BS spectra at varying energies of the resin region showing the $^{12}\text{C}(p,p_0)^{12}\text{C}$ resonance at 1734 keV; *Below:* BS spectra at 1.9 MeV for three areas marked on the Si PIXE map (above, left). (See Bailey *et al*, *Nucl. Instrum. Methods B* **267**, 2009, 2219 [279]). Reproduced from Fig.1 of [279]



This sort of mapping microbeam data is effectively a 3-D (three-dimensional) data cube, with 128x128 pixels and a PIXE and BS spectrum pair for each pixel. The data cube, intractable as it stands, can be analysed into its principal components (one of which is shown in Fig.29) by using a multivariate image analysis program such as AXSIA ("Automated eXpert Spectral Image Analysis [280]). These principal components are determined in the spatial domain [281] each giving a pair of PIXE/BS spectra characteristic for a given area of the map, and which can be directly interpreted by DataFurnace. The results of such an analysis are shown in Fig.30. In principle, the depth profile at each pixel can be reconstructed

from a linear combination of the principal components, thereby completely solving the 3-D structure of the sample.

Figure 29. One component from the principal component decomposition of the data cube of Fig.28 using AXSIA (see Doyle *et al.*, *Nucl. Instrum. Methods B* **249**, 2006, 828 [280]). This component is one of the several Si-rich components. Reproduced from Fig.2 of [275].

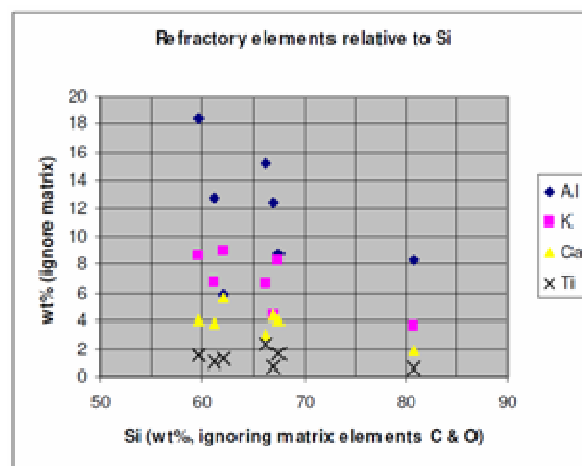


6.4. Mapping and tomography

Much of the PIXE literature already cited is for microbeam applications. This is accentuated for modern applications since PIXE on its own is analytically very similar to XRF, and cheap desktop XRF tools are now available. The great advantage of PIXE is the ease with which a microbeam can be formed; for XRF, polycapillary lenses are needed: these are not cheap and they have rather poor transmission, and so the probe size available is still not much below 20 μm . For PIXE, 1 μm microbeams have been routine for nearly twenty years, and there are persistent promises of much smaller beams. But a 2001 review points out that it has been much harder than expected to get smaller beams: with only a few reports at 500 nm [282]. Nevertheless, several groups are working on beamlines designed to give deep sub-micron spot sizes [283]. The Singapore group have shown that low current beams down to about 20 nm are feasi-

ble (see Fig.31): PIXE microscopy should be feasible at 100 nm resolution.

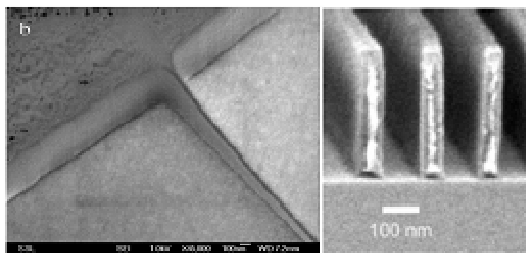
Figure 30. Composition plot of the abundance of minor elements relative to silicon in seven principal components of a mapped carbonaceous inclusion of a Darwin glass sample (see Fig.28) analysed by DataFurnace from a decomposition of the data cube by AXSIA; see Fig.29 and text. Reproduced from Fig.3 of [275].



The Darwin glass example in the last section points towards tomography. X-ray tomography (XR-T) is already established (see a recent description of a computed tomography system [284], a recent application on sea-urchin teeth [285], and a direct comparison of XR-T with IBA [286]), and STIM-T is an almost equivalent (and solved) problem [287]. Great strides have also been made towards a PIXE-T (see the summary in a recent review [288]), which is qualitatively much more complex than STIM-T (or, equivalently, XR-T). We have shown that in principle IBA-T (that is, using the BS signals as well as the PIXE signals) is already achievable in principle, and should be significantly more efficient (and therefore much faster!) than pure PIXE-T since a single slice already has (nearly) complete 3-D information. This is important since tomography is rather slow, and its importance is increased since it seems that beam damage severely limits the use of a pure PIXE-T for important classes of samples [289]. In principle, using the depth information available explicitly in IBA-T (from the particle signals) must be quicker than unfolding the depth information

available only implicitly (and at much lower resolution) in the PIXE signals.

Figure 31. *Left:* 22 nm line written in 850 nm thick HSQ^{XXVI} with a 1 MeV proton beam and an aspect ratio of about 37. Reproduced from Fig.3 of van Kan *et al* (2006) [290]; *Right:* Parallel lines written in 350 nm thick PMMA with a 2 MeV proton beam and an aspect ratio of about 7. Reproduced from Fig.4 of van Kan *et al* (2004) [291]



6.5. Summary

Thin film depth profiling using MeV-IBA is a major application field for small accelerators. We have here briefly reviewed it, giving a flavour for its development and history, and giving summary details of the critical parameters (theory and databases) needed to obtain reliable analyses. (A further fine review from a different point of view has also recently appeared [292].)

Unusually, we have covered both the photon and the particle techniques in a unified approach, for the reason that we wish to emphasise the enormous benefit available from treating spectra from multiple techniques self-consistently.

There have been really dramatic advances over the last decade in the detailed implementation and in the reliability of the IBA codes used, also in the new availability of reliable EBS cross-sections, and therefore we believe that the approach we are

sketching has really only become feasible in the last five years or so.

A modern treatment of IBA spectra would expect to extract depth profiles which give calculated spectra effectively identical to the data: thus we are now usually able to extract from the spectra almost all the information they contain. Where photon or particle spectra separately are ambiguous, jointly analysed (perhaps with multiple energies or beams or geometries) they become unambiguous.

We even expect that systematic procedures could be found to do this analysis pixel by pixel with the microbeam, with the ultimate prize of IBA tomography (IBA-T). Where X-ray tomography (or, equivalently, STIM-T) are now standard techniques, PIXE-T is feasible in principle but so slow in practice that most samples are destroyed by the beam. But IBA-T should be (at least) an order of magnitude faster, since the backscattering signal enables the depth information to be unfolded directly from the PIXE data.

We hope that the new power of these old techniques will inspire a new generation of analysts.

Acknowledgments

CJ wishes to thank B.L.Doyle, A.F.Gurbich, N.P.Barradas, M.A.Reis, and E.Szilágyi for helpful comments, and D.Jeseršek for pointing him to Newton's use of the word "spectrum". Surrey Ion Beam Centre is supported by the European Community as a TransNational Access Infrastructure of the Integrating Activity «Support of Public and Industrial Research Using Ion Beam Technology (SPIRIT)» under EC contract no. 227012. We also acknowledge the support of EPSRC through contract EP/D032210/1 and various EPSRC contracts in the UK academic community.

^{XXVI} PMMA: poly-methyl methacrylate; HSQ: hydrogen silsesquioxane. Note that electron-beam lithography feature size and aspect ratio are both limited by the proximity effect, and deep UV lithography is limited by diffraction effects. These structures cannot be formed by e-beam or UV lithography. Note also that although the e-beam spot size in SEM can be nanometres, the X-ray SEM-EDS maps have a resolution given by the e-beam interaction volume, typically microns. For PIXE the interaction volume is defined by the beam spot size.

Table 1. RBS/EBS Boundary for Protons: where cross-section differs from Rutherford by 4%.

The optical model ("OM") calculations of Bozoian [3] [4] [38] are compared with "Data" from either IBANDL (www-nds.iaea.org/ibandl), or SigmaCalc (www-nds.iaea.org/sigmacalc) calculations of Gurbich [44] [45] for a head-on collision. The position of the first resonance ("1st R") in the (p,p) elastic cross-section is shown, and the minimum energy for which data are available is also shown, distinguishing between SigmaCalc ("σ_{calc}") and measured data ("Data"). The value of the (p,p) cross-section relative to Rutherford at this minimum value ("σ (rtr)") is also shown.

The "optical model" calculation is approximated by $Z_2(M_1+M_2)/(10M_2)$ [4].

Z	A	Estimate 4% deviation		1 st R	Minimum database energy (May 2011)		σ (rtr)	Comment	
		OM	Data		σ _{calc}	Data			
		keV	keV	keV	keV	keV			
2	He	4	250			1600	90	(No data available)	
3	Li	6	350	600	1400	500	1.01	Data at 156.7°	
3	Li	7	343	407	440	373	1	Data at 81.3°	
4	Be	9	444	219	257	143	1	Data at 170°	
5	B	10	550	<500		500	1.24	Data at 170°	
5	B	11	545	<500	525	500	1.35	Data at 170°	
6	C	12	650	<360	440	360	1.04	SigmaCalc at 180°	
7	N	14	750	400	1003	300	1.01	SigmaCalc at 180°	
7	N	15	747		415			p,αγ resonance, no EBS data	
8	O	16	850	<100	280	100	0.95	SigmaCalc at 180°	
8	O	18	844	<590(?)	620(?)	590	0.88	Data at 138.7°: strong resonance at 800 keV	
9	F	19	947	552	623	552	0.95	SigmaCalc at 180°	
10	Ne	20	1050	<1500	1160	1500	1.28	SigmaCalc at 180°: strong p,γ resonance at 1160 keV	
10	Ne	22	1045	<<1574	1588	1574	0.1	Data at 150°: clear p,p ₀ resonance at 1700 keV; strong p,p ₁ resonance at 2130 keV	
11	Na	23	1148	573	593	573	0.96	SigmaCalc at 180°	
12	Mg	24	1250	700	821	700	400	1	SigmaCalc at 180°
13	Al	27	1348	936	937	900	500	1	SigmaCalc at 180°
14	Si	28	1450	1272	1608	1000	0.99	SigmaCalc at 180°	
14	Si	29	1448	1219	1333	1219		Relative data at 140°	
14	Si	30	1447	<1007	1018	1007	0.87	Data at 140°: strong resonance at 1290 keV	
15	P	31	1548	1175	1251	1000	1	SigmaCalc at 180°	
16	S	32	1650	1790	1889	1506	1	SigmaCalc at 180°	
17	Cl	35	1749	1326	2100	1320	1.02	Data at 150°	
17	Cl	37	1746	1338	1338	1130	1	Data at 172°	
18	Ar	40	1845	1810	1858	1723	1020	1	SigmaCalc at 180°
19	K	39	1949	<1731	1770	1731	0.95	SigmaCalc at 180°	
20	Ca	40	2050	2159	2383	1799	0.99	SigmaCalc at 180°	
22	Ti	48	2246	1901	1901	1811	1	SigmaCalc at 180°	
24	Cr	52	2446	<2600	2600	3200	2400	0.57	SigmaCalc at 180°; relative data at 141° shows strong resonance at 2600 keV
27	Fe	56	2850	2050	2051	2011	0.993	SigmaCalc at 180°	

Appendix A: Glossary of IBA techniques

- ANN Artificial neural networks. Black boxes containing image recognition software (and no physics!) that instantly recognises (without calculation) features of spectra (layer thicknesses etc). The performance of ANNs depends critically on their training.
- BS (Elastic) backscattering. Can be either RBS or EBS.
- Blocking: Inverse of channelling. Crystal channels have high transparency to collimated ion beams, major axis strings of atoms block the ion beam.
- CAICISS: Coaxial impact collision ISS. A variety of LEIS.
- Channelling: Damage in single crystals is frequently quantified with ion channelling, where the well collimated ion beam is aligned with major crystallographic axes. Can readily be used with STIM, PIXE, BS, NRA. Channelling and blocking patterns are essential to MEIS.
- EBS Elastic (non-Rutherford) backscattering. Scattering cross-section is given by the the elastic scattering channel of the reaction, and depends on the nuclear structure of the two nuclei. Cross-section can be calculated by R-matrix or other methods which have nuclear data (energy levels etc) as input, but the calculations must be informed by direct cross-section measurements. Measurements and evaluations are on the IBANDL website.
- EDS Energy dispersive (X-ray) spectrometry.
- ERD Elastic recoil detection. Follows the recoiled rather than the scattered ion in the elastic collision. He-ERD is valuable for analysing H isotopes. HI-ERD (heavy ion ERD) typically uses primary beams of ~1 MeV/amu, and ToF (time of flight) or gas detectors for the heavy recoils.
- ERDA Elastic recoil detection analysis. Synonym for ERD and preferred in Finland, sounding better in Finnish
- FIB Focussed ion beam. See SIMS.
- FRS Forward recoil spectrometry. Synonym for ERD.
- HI-ERD Heavy ion ERD. Gas ionisation or ToF detectors, and energies comparable to 1 MeV/nucleon are usually used.
- HI-RBS Heavy ion RBS (gas ionisation detectors are ideal). A Li beam is often used for better mass resolution.
- IBA MeV Ion Beam Analysis, including STIM, IBIL, PIXE, BS (RBS or EBS), ERD, NRA, PIGE, MeV-SIMS. MEIS and LEIS are lower energy versions of RBS. Commercial SIMS instruments use keV energy primary beams.
- IBIC Ion beam induced current. Low fluence technique for non-destructively characterising semiconductor device quality: carrier lifetime, carrier mobility, charge trapping defects etc. Ion analogue of EBIC and XBIC.
- IBIL Ion beam induced luminescence. The ion analogue of cathodoluminescence (electron-induced) and photoluminescence.
- ISS Ion scattering spectrometry. Synonym for one of LEIS, MEIS, RBS, depending on the energy regime.
- LEIS Low energy ion scattering. RBS using keV ion beams. New high sensitivity detectors make this a rapid technique which looks at the outermost layer of the sample. Thus complementary (with higher depth resolution) to XPS.
- MEIS Medium energy ion scattering. RBS using ~100 keV ion beams. Gives information on the crystallography and composition of the near-surface region (~100nm).
- Microbeam Ion beams can be readily focussed with quadrupole triplets (or multiplets) to a focus of ~1 μm . It is thought that 100 nm is feasible for PIXE and 30 nm is feasible for STIM.
- NRA (Inelastic) nuclear reaction analysis. NRA cross-sections can also be calculated (as well as measured of course) and a few evaluations are on the IBANDL website together with many measured cross-sections.
- PDMS Plasma desorption mass spectrometry. Forerunner of MALDI
- PESA Proton elastic scattering analysis. Synonym for proton EBS, except that PESA can also be at forward angles.
- PIGE Particle induced gamma ray emission. A special case of NRA where a gamma ray results.
- PIXE Particle induced X-ray emission. The ion analogue of XRF or, since today PIXE is usually used with a scanning microbeam, SEM-EDS or EPMA. Note that EPMA is also PIXE, since electrons are also particles!
- RBS Rutherford backscattering spectrometry. Scattering cross-section is analytical, and given by the Coulomb potential (with screening). Ion analogue of the BSE signal in SEM. Switches to EBS when the Coulomb barrier is increased. Called MEIS for beams near the stopping power maximum (~100 keV), and LEIS for keV beams.
- SIM Scanning ion microscopy. Ion analogue of SEM.
- SIMS Secondary ion mass spectrometry. Another form of IBA using (for example) a 30 keV ion source for sputtering. The secondary (sputtered) ions are mass analysed. One important variant is FIB (focussed ion beam machining) which uses a high intensity (and very bright) nano-focussed liquid metal ion source (usually Ga): another is MeV-SIMS, where the sputtering results from electronic energy loss, not the nuclear collision cascade.
- STIM Scanning transmission ion microscopy. Typically looks at the energy loss of primary beam particles transmitted through thin samples, so that it is similar to EELS in the TEM (but with much lower energy resolution).
- ToF Time of flight. ToF-SIMS and ToF-ERD are standard techniques
- WDX Wavelength dispersive X-ray spectrometry (high resolution).

Appendix B: Glossary of related techniques

- AES** Auger electron spectrometry. Also SAM: scanning Auger microscopy. Electrons in, electrons out. Same electron spectrometer as XPS, same EMFP, thus also a true surface technique. AES is really SEM in UHV (ultra-high vacuum), but looking at the (high energy) Auger electrons rather than the number of (low energy) secondary electrons. Chemical shifts are also present in AES, but are more complex than in XPS.
- AFM** Atomic force microscopy. One of a number of scanning probe microscopies, including the original STM (scanning tunnelling microscopy).
- AMS** Accelerator mass spectrometry. A form of IBA (the accelerator is the same) where the sample goes in the source. Used routinely for ^{14}C and similar isotopic analyses.
- BSE** Backscattered electron signal available on SEMs. This carries qualitative Z-contrast.
- DESI** Desorption electrospray ionisation. As MALDI.
- DART** Direct analysis in real time. As MALDI.
- EBIC** Electron beam induced current. Analogue of IBIC.
- EDS** Energy dispersive X-ray spectrometry ("EDX" is a tradename). Usually used as "SEM-EDS".
- EELS** Electron energy loss spectrometry. A TEM technique. See XAS.
- EPMA** Electron probe microanalysis: just an SEM specialised for X-ray analysis, generally with one or more WDXs (wavelength dispersive X-ray spectrometers). See also SEM-EDS.
- ESCA** Electron spectroscopy for chemical analysis. The photoelectron process can show pronounced chemical shifts for difference valence states. Synonym for XPS.
- EXAFS** Extended X-ray absorption fine structure. Incident X-ray energy $\sim 50\text{ eV} - \sim 1000\text{ eV}$ above the absorption edge, giving high energy photoelectrons for which *single* scattering dominates. See NEXAFS and XAS.
- FTIR** Fourier transform infra-red spectrometry. One of a large class of emission and absorption spectrometries sensitive, like Raman spectroscopy, to atomic and molecular vibration modes.
- ICP-MS** Inductively coupled plasma mass spectrometry. One of a large class of mass spectrometries sensitive to ng/g (and better) where PIXE is only sensitive to mg/kg (at best). But ICP-MS analyses trace elements in bulk samples whose gross composition is known.
- LEED** Low energy electron diffraction. Often used as a surface monitor in UHV (ultra-high vacuum) deposition systems.
- MALDI** Matrix-assisted laser desorption ionization. An in-air spectrometry sensitive to molecules of high molecular weight. SIMS (with keV ions) must be done in vacuum; also gives molecular ions, but is a much more energetic sputtering technique and fragments the sputtered ions more for larger molecules.
- NEXAFS** Near-edge extended X-ray absorption fine structure. Incident X-ray energy $\sim 10\text{ eV} - \sim 50\text{ eV}$ above the absorption edge, giving low energy photoelectrons for which *multiple* scattering dominates. See EXAFS and XAS.
- NMR** Nuclear magnetic resonance or MRI (magnetic resonance imaging) in imaging mode.
- SAM** Scanning AES.
- SEM** Scanning electron microscopy for imaging surface topography, primarily looking at the secondary electron signal. Often comes with EDS (or EDX: energy dispersive X-ray spectrometry) and often has a BSE (backscattered electron) signal too. The X-ray detector is the same as usually used for PIXE. The scanning ion microbeam (SIM) is thus an analogue of SEM, EDS and BSE being analogues of PIXE and EBS. And often an secondary electron detector is included in an SIM chamber to see the topography directly.
- TEM** Transmission electron microscopy for imaging in both real and reciprocal space: always includes SAD (selected area electron diffraction). Also XTEM for cross-sectional TEM, and HR-TEM for high (atomic) resolution TEM. Often has EDS and EELS.
- WDX** Wavelength dispersive X-ray spectrometry. Very high energy resolution is available. See EDS and EPMA.
- XANES** X-ray absorption near-edge structure. In the XANES region the energy of the incident beam is $\sim 10\text{ eV}$ from the absorption edge, and transitions of core electrons to non-bound levels with close energy occur with high probability. See XAS.
- XAS** X-ray absorption spectrometry. See EELS for the low resolution TEM technique. See XANES, NEXAFS and EXAFS for the high resolution synchrotron techniques which need high intensity monochromatic beams.
- XBIC** X-ray beam induced charge (synchrotron technique). Analogue of IBIC.
- XPS** X-ray photoelectron spectrometry. X-rays in, photoelectrons out. Because the EMFP (electron mean free path) is only a few nm this is a true surface technique, but sputtering is frequently used to give depth profiles. Synonym for ESCA.
- XRD** X-ray diffraction for observing crystalline structure. A very wide variety of methods are in use including thin-film variants.
- XRF** X-ray fluorescence. Like PIXE and EPMA but excited by X-rays. Same physics as XPS & AES but looks at the X-ray resultant, not the Auger or photo-electron one, and is therefore a "bulk", not a surface technique.

References

- 1 "A Letter of Mr. Isaac Newton, Mathematick Professor in the University of Cambridge; containing his New Theory about Light and Colors [*sic*] : Where Light is declared to be not Similar or Homogeneous, but consisting of difform rays, some of which are more refrangible than others : And Colors are affirm'd to be not Qualifications of Light, derived from Refractions of natural Bodies, (as 'tis generally believed ;) but Original and Connate properties, which in divers rays are divers ; Where several Observations and Experiments are alledged to prove the said Theory." *Philosophical Transactions* 6 (February 19. 1671/72) 3075-3087

- 2 J.W.Mayer & E.Rimini (ed) *Ion Beam Handbook for Materials Analysis* (1977, New York: Academic). Product of the previous IBA conference at Catania.
- 3 J.R.Tesmer & M.Nastasi (eds) *Handbook of Modern Ion Beam Analysis* (1995, Pittsburgh: Mat. Res. Soc.)
- 4 Y.Q.Wang and M.Nastasi (eds.) *2010 Handbook of Modern Ion Beam Analysis* (2nd Edition, Pittsburgh: MRS)
- 5 J.W.Mayer, J.F.Ziegler (eds.) *Proc. Int. Conf. on Ion Beam Surface Layer Analysis* (Yorktown Heights, NY, 18-20 June 1973) *Thin Solid Films* **19** (Dec.1973)
- 6 Roger Webb, Melanie Bailey, Chris Jeynes & Geoff Grime (eds.), 12th International Conference on Ion Beam Analysis (Univ. Cambridge, 7-11 September 2009), *Nucl. Instrum. Methods B*, **268** (2010) 1703-2216
- 7 G.W.Grime (ed.), 19th International Conference on Particle-induced X-ray emission and its analytical applications (Univ.Surrey, 27th June – 2nd July 2010) *X-Ray Spectrometry* **40** (2011) 119–234
- 8 L.Giuntini, A review of external microbeams for ion beam analyses, *Anal.Bioanal.Chem.* **401** (2011) 785-793
- 9 H.Geiger & E.Marsden, On a Diffuse Reflection of the α -Particles. *Proc. Roy. Soc. Series A*, **82** (1909) 495–500
- 10 E.Rutherford, The Scattering of α and β Particles by Matter and the Structure of the Atom, *Philos. Mag. Series 6*, **21** (May 1911) 669–688
- 11 J.Chadwick, E.S.Bieler, The collisions of alpha particles with hydrogen nuclei, *Philos. Mag. Series 6*, **42** (1921) 923-940
- 12 N. F. Mott, The collision between two electrons, *Proc. Roy. Soc. A*, **126** (1930) 259-267
- 13 C.Gerthsen, Streuungsmessungen von H-Strahlen in Wasserstoff als Beitrag zur Klärung ihrer Wellennatur (The dispersion measurements of H-rays in hydrogen as a contribution to the clarification of their wave nature), *Annalen der Physik*, **401** (1931) 769-786.
- 14 M.A.Tuve, N.P.Heydenburg, L.R.Hafstad, The Scattering of Protons by Protons, *Phys. Rev.*, **50** (1936) 806-825
- 15 G. Breit, E. U. Condon, R. D. Present, Theory of Scattering of Protons by Protons, *Phys. Rev.*, **50** (1936) 825-845
- 16 R. A. Laubenstein, M. J. Laubenstein, L. J. Koester, R. C. Mobley, The Elastic Scattering and Capture of Protons by Oxygen, *Phys. Rev.*, **84** (1951) 12-18
- 17 S.Rubin, T.O.Passell, E.Bailey, The chemical analysis of surfaces by nuclear methods, *Anal.Chem.* **29** (1957) 736-743
- 18 J.A. Davies, G. Amsel, J.W. Mayer, Reflections and reminiscences from the early history of RBS, NRA and channeling, *Nucl. Instrum. Methods B*, **64** (1992) 12-28
- 19 G.Amsel, P.Baruch, O.Smulkowski, Detecteur de particules lourdes jonction n-p au silicium, *Nucl. Instrum. Methods* **8** (1960) 92-105
- 20 A.Turkevich, Chemical Analysis of Surfaces by Use of Large Angle Scattering of Heavy Charged Particles, *Science*, **134** (1961) 672-674
- 21 Anthony L. Turkevich, Ernest J. Franzgrote, James H. Patterson, Chemical Analysis of the Moon at the Surveyor V Landing Site, *Science*, **158** (1967) 635-637
- 22 J.Gyulai, O.Meyer, J.W.Mayer, Analysis of silicon nitride layers on silicon by backscattering and channeling effect measurements, *Appl. Phys. Lett.*, **16** (1970) 232-234
- 23 W.H.Bragg & R.Kleeman, The α particles of radium and their loss of range in passing through various atoms and molecules. *Philos. Mag.* **10** (1905) 318
- 24 The SRIM (Stopping and Ranges of Ions in Matter) website <http://www.srim.org> (downloaded 21st July 2011)
- 25 J. F. Ziegler, "SRIM-2003", *Nucl. Instrum. Methods B*, **219** (2004) 1027-1036
- 26 J.F.Ziegler, J.P.Biersack, M.D.Ziegler, *SRIM - The Stopping and Range of Ions in Matter*, 2008, (published by print-to-order) <http://www.lulu.com/content/1524197>
- 27 H.Paul, "Stopping Power for Light Ions" (downloaded 21 July 2011) <http://www.exphys.uni-linz.ac.at/stopping/>
- 28 H.Paul, Recent results in stopping power for positive ions, and some critical comments, *Nucl. Instrum. Methods B*, **268** (2010) 3421–3425
- 29 P.D.Bourland, D.Powers, Bragg-Rule Applicability to Stopping Cross Sections of Gases for alpha Particles of Energy 0.3-2.0 MeV, *Phys. Rev. B*, **3** (1971) 3635.3641
- 30 M.Msimanga, C.M.Comrie, C.A.Pineda-Vargas, S.Murray, Experimental stopping powers of Al, Mg, F and O ions in ZrO₂ in the 0.1–0.6 MeV/u energy range, *Nucl. Instrum. Methods B*, **268** (2010) 1772-1775
- 31 Z.Siketić, I.Bogdanović Radović, E.Alves, N.P.Barradas, Stopping power of ¹¹B in Si and TiO₂ measured with a bulk sample method and Bayesian inference data analysis, *Nucl. Instrum. Methods B*, **268** (2010) 1768-1771
- 32 S.Damache, D.Moussa, S.Ouichaoui, Stopping of ~0.2–3.4 MeV/amu ¹H⁺ and ⁴He⁺ ions in polyvinyl formal, *Nucl. Instrum. Methods B*, **268** (2010) 1759-1762
- 33 James F. Ziegler, M.D.Ziegler, J.P.Biersack, SRIM – The stopping and range of ions in matter (2010), *Nucl. Instrum. Methods B*, **268** (2010) 1818-1823
- 34 H.Geiger & E.Marsden, The laws of deflexion of α particles through large angles. *Philos. Mag. Series 6*, **25** (1913) 604
- 35 J.B.Marion, F.C.Young, *Nuclear Reaction Analysis, Graphs and Tables*, 1968 (Wiley: New York)
- 36 H.H.Andersen, F.Besenbacher, P.Loftager, W.Möller, Large-angle scattering of light ions in the weakly screened Rutherford region, *Phys.Rev.A*, **21** (1980) 1891-1901
- 37 C. Jeynes, N. P. Barradas, H. Rafla-Yuan, B. P. Hichwa, R. Close, Accurate depth profiling of complex optical coatings, *Surf. Interface Anal.* **30** (2000) 237–242
- 38 M.Bozoian, K.M.Hubbard, M.Nastasi, Deviations from Rutherford-scattering cross sections, *Nucl. Instrum. Methods B*, **51** (1990) 311-319
- 39 A.F.Gurbich, On the concept of an actual Coulomb barrier, *Nucl. Instrum. Methods B*, **217** (2004) 183–186
- 40 D. Abriola, A.F.Gurbich, M.Kokkoris, A.Lagoyannis, V.Paneta, Proton elastic scattering differential cross-sections for ¹²C, *Nucl. Instrum. Methods B*, **269** (2011) 2011-2016
- 41 R.E.Azuma, E.Uberseder, E.C.Simpson, C.R.Brune, H.Costantini, R.J.de Boer, J.Görres, M.Heil, P.J.LeBlanc, C.Ugalde, M.Wiescher, AZURE: An R-matrix code for nuclear astrophysics, *Phys.Rev.C*, **81** (2010) 045805
- 42 <http://www-nds.iaea.org/iba/> (downloaded 21 July 2011) Development of a reference database for IBA, *An IAEA Nuclear Data Section Co-ordinated Research Project* 2005-2009 (F41023)
- 43 D.Abriola, N.P.Barradas, I.Bogdanović-Radović, M.Chiari, A.F.Gurbich, C.Jeynes, M.Kokkoris, M.Mayer, A.R.Ramos, L.Shi, I.Vickridge, Development of a refer-

- ence database for Ion Beam Analysis and future perspectives, *Nucl. Instrum. Methods B*, **269** (2011) 2011-2016
- 44 A.F.Gurbich, Evaluated differential cross-sections for IBA, *Nucl. Instrum. Methods B*, **268** (2010) 1703-1710
- 45 A.F.Gurbich, "The interaction of charged particles with nuclei", Chapter 3 in *2010 Handbook of Modern IBA* (Y.Q.Wang & M.Nastasi, eds, 2nd Ed., Pittsburgh: MRS)
- 46 A.F. Gurbich, I.Bogdanović Radović, Z.Siketić, M.Jakšić, Measurements and evaluation of the cross-section for helium elastic scattering from nitrogen, *Nucl. Instrum. Methods B*, **269** (2011) 40-44
- 47 A.F.Gurbich, C.Jeynes, Evaluation of non-Rutherford proton elastic scattering cross-section for magnesium, *Nucl. Instrum. Methods B*, **265** (2007) 447-452
- 48 N.P.Barradas, E.Alves, C.Jeynes, M.Tosaki, Accurate simulation of backscattering spectra in the presence of sharp resonances, *Nucl. Instrum. Methods B*, **247** (2006) 381-389
- 49 J.L'Ecuyer, C.Brassard, C.Cardinal, J.Chabbal, L.Deschênes, J.P.Labrie, B.Terreault, J.G.Martel, R.St.-Jacques, An accurate and sensitive method for the determination of the depth distribution of light elements in heavy materials, *J.Appl.Phys.*, **47** (1976) 381-382
- 50 G.Dollinger, C.M.Frey, A.Bergmaier, T.Faestermann, Elastic recoil detection with single atomic layer depth resolution, *Nucl. Instrum. Methods B*, **136-138** (1998) 603-610
- 51 E. Szilágyi, On the limitations introduced by energy spread in elastic recoil detection analysis, *Nucl. Instrum. Methods B*, **183** (2001) 25-33
- 52 M. Döbeli, C.Kottler, F.Glaus, M.Suter, ERDA at the low energy limit, *Nucl. Instrum. Methods B*, **241** (2005) 428-435
- 53 B.Brijs, T.Sajavaara, S.Giangrandia, T.Janssens, T.Conard, K.Arstila, K.Nakajima, K.Kimura, A.Bergmaier, G.Dollinger, A.Vantomme, W.Vandervorst, The analysis of a thin SiO₂/Si₃N₄/SiO₂ stack: A comparative study of low-energy heavy ion elastic recoil detection, high-resolution Rutherford backscattering and secondary ion mass spectrometry, *Nucl. Instrum. Methods B*, **249** (2006) 847-850
- 54 E. Szilágyi, F. Pászti, V. Quillet, F. Abel, Optimization of the depth resolution in ERDA of H using ¹²C ions, *Nucl. Instrum. Methods B*, **85** (1994) 63-67
- 55 James F. Browning, Robert A. Langley, Barney L. Doyle, James C. Banks, William R. Wampler, High accuracy, high energy He-ERD analysis of H, D and T, *Nucl. Instrum. Methods B*, **161-163** (2000) 211-215
- 56 J.C.Banks, J.F.Browning, W.R.Wampler, B.L.Doyle, C.A.LaDuca, J.R.Tesmer, C.J.Wetteland, Y.Q.Wang, Round robin analyses of hydrogen isotope thin films standards, *Nucl. Instrum. Methods B*, **219-220** (2004) 444-449
- 57 G.Boudreault, R.G.Elliman, R.Grötzschel, S.C.Gujrathi, C.Jeynes, W.N.Lennard, E.Rauhala, T.Sajavaara, H.Timmers, Y.Q.Wang, T.D.M.Weijers, Round Robin: measurement of H implantation distributions in Si by elastic recoil detection, *Nucl. Instrum. Methods B*, **222** (2004) 547-566
- 58 B.L.Doyle, P.S.Peercy, Technique for profiling ¹H with 2.5 MeV (*sic*) Van de Graaff accelerators, *Appl. Phys. Lett.*, **34** (1979) 811
- 59 F.Pászti, E.Kótai, G.Mezey, A.Manuaba, L.Pócs, D.Hildebrandt, H.Strusny, Hydrogen and deuterium measurements by elastic recoil detection using alpha particles, *Nucl. Instrum. Methods B*, **15** (1986) 486-491
- 60 N.P.Barradas, S.A.Almeida, C.Jeynes, A.P.Knights, S.R.P.Silva, B.J.Sealy, RBS and ERDA study of ion beam synthesised amorphous gallium nitride, *Nucl. Instrum. Methods B*, **148** (1999) 463-467
- 61 H.Timmers, R.G.Elliman, T.R.Ophel, New design features of gas ionization detectors used for elastic recoil detection, *Nucl. Instrum. Methods A*, **447** (2000) 536-543
- 62 M.Malpell, M.Döbeli, M.Suter, Annular gas ionization detector for low energy heavy ion backscattering spectrometry, *Nucl. Instrum. Methods B*, **267** (2009) 1193-1198
- 63 P.Reichart, G.Datzmann, A.Hauptner, R.Hertenberger, C.Wild, G.Dollinger, Three-dimensional hydrogen microscopy in diamond, *Science* **306** (2004) 1537-1540
- 64 E Rutherford, Collision of particles with light atoms. IV An anomalous effect in nitrogen, *Phil. Mag.* **37** (1919) 581-587
- 65 E.Rutherford, J.Chadwick, The disintegration of elements by alpha particles, *Phil.Mag.* **44** (1922) 417-432
- 66 J.D.Cockcroft, E.T.S.Walton, Disintegration of lithium by swift protons, *Nature* **129** (1932) 649-649
- 67 W.E.Sweeney Jr, J.B.Marion, Gamma-ray transitions involving isobaric-spin mixed states in Be⁸, *Phys.Rev.* **182** (1969) 1007-1021
- 68 See the Q-value calculators at (for example) <http://nucldata.nuclear.lu.se/database/masses/> or <http://www.nndc.bnl.gov/qcalc/>
- 69 I.C.Vickridge, I.Trimaille, J.-J.Ganem, S.Rigo, C.Radtke, I.J.R.Baumvol, F.C.Stedile, Limiting Step Involved in the Thermal Growth of Silicon Oxide Films on Silicon Carbide *Phys. Rev. Lett.* **89** (2002) 256102 [4 pages]
- 70 A.P.Matthews, C.Jeynes, K.J.Reeson, J.Thornton, N.M.Spyrou, Quantification of the separate matrix constituents of spheroidal graphite cast iron implanted with ¹⁵N by nuclear reaction analysis using an ion microprobe, *Nucl. Instrum. Methods B*, **64** (1992) 452-456
- 71 <http://www-nds.iaea.org/pige/publicPIGE.html> (downloaded 21 July 2011): IAEA Coordinated Research Project on "Reference Database for Particle-Induced Gamma ray Emission (PIGE) Spectroscopy"
- 72 J.Stark, G.Wendt, Über das Eindringen von Kanalstrahlen in feste Körper (The penetration of canal rays in solid bodies), *Annalen der Physik*, **343** (1912) 921-940
- 73 M.M.Bredov, I.M.Okuneva, The depth of penetration of matter by moderate energy ions, *Sov. Phys. Dok.* **113** (1957) 795-796
- 74 B.Domeij, I.Bergstrom, J.A.Davies, J.Uhler, A method of determining heavy ion ranges by analysis of alpha-line shapes, *Arkiv for Fysik* **24** (1963) 399-411
- 75 L.Eriksson, J.A.Davies, J.Denhartog, J.W.Mayer, O.J.Marsh, R.Markariou, Analysis of Sb-implanted silicon by (p,p) scattering and Hall measurements, *Appl.Phys.Lett.* **10** (1967) 323-325
- 76 M.T.Robinson, O.S.Oen, Computer studies of slowing down of energetic atoms in crystals *Phys. Rev.* **132** (1963) 2385-2398
- 77 E. Kótai, Measurement of the stopping powers for channeled ions in ion implanted crystals, *Nucl. Instrum. Methods B*, **118** (1996) 43-46
- 78 J.Lindhard, Influence of crystal lattice on motion of energetic charged particles, *K. Dan. Vidensk. Selsk. Mat. Fys. Medd.* **34**(14) (1965) 1.

- 79 C.W.Rischau, C.S.Schnohr, E.Wendler, W.Wesch, Ion-beam-induced damage formation in CdTe, *J.Appl.Phys.* **109** (2011) 113531
- 80 K. Gärtner, Modified master equation approach of axial dechanneling in perfect compound crystals, *Nucl. Instrum. Methods B*, **227** (2005) 522-530
- 81 V.S.Drumm, A.D.C.Alves, J.O.Orwa, D.N.Jamieson, J.C.McCallum, S.Prawer, C.C.G.Ryan, Lattice location of nickel in diamond by RBS channelling and PIXE, *Phys.Stat.Sol. A*, **208** (2011) 42-46
- 82 L.Rebouta, P.J.M.Smulders, D.O.Boerma, F.Aguiló-Lopez, M.F. da Silva, J.C.Soaes, Ion-beam channeling yields of host and impurity atoms in LiNbO₃. Computer simulations, *Phys. Rev. B*, **48** (1993) 3600-3610
- 83 A.Kling, CASSIS — A new Monte-Carlo computer program for channeling simulation of RBS, NRA and PIXE, *Nucl. Instrum. Methods B*, **102** (1995) 141-144
- 84 E. Kótai, RBX, Computer methods for analysis and simulation of RBS and ERDA spectra, *Proc. 14th Int. Conf. on the Application of Accelerators in Research and Industry*, Nov 6-9, 1996, Denton, Texas USA, **CP392**, J.L. Duggan & I.L. Morgan eds. (AIP Press, New York 1997) 631-634
- 85 C.Jeynes, K.E.Puttick, L.C.Whitmore, K.Gärtner, A.E.Gee, D.K.Millen, R.P.Webb, R.M.A.Peel, B.J.Sealy, Laterally resolved crystalline damage in single-point-diamond-turned silicon, *Nucl. Instrum. Methods B*, **118** (1996) 431-436
- 86 D.P.Smith, Analysis of surface composition with low-energy backscattered ions, *Surf. Sci.* **25** (1971) 171-191
- 87 H.H.Brongersma, R.H.Bergmans, L.G.C.Buijs, J.-P.Jacobs, A.C.Kruseman, C.A.Severijns, R.G. van Welzenis, Developments in low-energy ion scattering from surfaces, *Nucl. Instrum. Methods B*, **68** (1992) 207-212
- 88 see the Calipso website for up-to-date information on this technique: <http://www.calipso.nl/>
- 89 H.R.J. ter Veen, T.Kim, I.E.Wachs, H.H.Brongersma, Applications of High Sensitivity-Low Energy Ion Scattering (HS-LEIS) in heterogeneous catalysis, *Catalysis Today* **140** (2009) 197-201
- 90 W.C.Turkenburg, W.Soszka, F.W.Saris, H.H.Kersten, B.G.Colenbrander, Surface structure analysis by means of Rutherford scattering methods to study surface relaxation, *Nucl. Instrum. Methods* **132** (1976) 587-602
- 91 H.H.Brongersma, M.Draxler, M. de Riddera, P.Bauer, Surface composition analysis by low-energy ion scattering, *Surface Science Reports* **62** (2007) 63-109
- 92 M.Walker, M.G.Brown, M.Draxler, M.G.Dowsett, C.F.McConville, T.C.Q.Noakes, P.Bailey, Structural analysis of the Cu(100)-p(2x2)-Sn surface using low and medium energy ion scattering spectroscopies, *Phys.Rev.B*, **83** (2011) 085424 (8pp)
- 93 J.C.Vickerman, A.Brown, N.M.Reed, *Secondary Ion Mass Spectrometry*, Oxford Science Publications (1989)
- 94 *ToF SIMS: Surface Analysis by Mass Spectrometry*, (Eds J.C.Vickerman & D.Briggs), IM Publications, ISBN 1-901019-03-9, 2001
- 95 R.Hill, P.Blenkinsop, S.Thompson, J.C.Vickerman J.S.Fletcher, A new ToF-SIMS instrument for 3D imaging and analysis *Surf. Int. Anal.*, **43** (2011) 506-509
- 96 John A. Kilner, Stephen J. Skinner, Hidde H. Brongersma, The isotope exchange depth profiling (IEDP) technique using SIMS and LEIS, *J Solid State Electrochem.* **15** (2011) 861-876
- 97 M.G.Dowsett, A.Adriaens, M.Soaes, H.Wouters, V.V.N.Palitsin, R. Gibbons, R.J.H.Morris, The use of ultra-low-energy dynamic SIMS in the study of the tarnishing of silver, *Nucl. Instr. Methods B*, **239** (2005) 51-64
- 98 J.Bertho, V.Stolijan, M.-L.Abel, J.F.Watts, The effect of silane incorporation on a metal adhesive interface: A study by EELS, *Micron* **41** (2010) 130-134
- 99 C.W.Magee, R.E.Honig, Depth profiling by SIMS: depth resolution, dynamic range and sensitivity, *Surface & Interface Analysis*, **4** (1982) 35-41
- 100 J.S.Fletcher, N.P.Lockyer, J.C.Vickerman, Developments in molecular SIMS depth profiling and 3D imaging of biological systems using polyatomic primary ions, *Mass Spectrom. Rev.* **30** (2011) 142-174
- 101 H.F. Arlinghaus, *Surface and Thin Film Analysis. Principles, Instrumentation, Applications*, (Eds H. Burbert, H. Jennete), Wiley-VCH; Weinheim (2002) 132-141
- 102 D.F.Torgerson, R.P.Skowronski, R.D.Macfarlane, A new approach to mass spectroscopy of non-volatile compounds, *Biochem. & Biophys. Res. Commun.* **60** (1974) 616-621
- 103 R.D.Macfarlane, Mass Spectrometry of Biomolecules: From PDMS to MALDI, *Brazilian Journal of Physics*, **29** (1999) 415-421
- 104 Y.Nakata, Y.Honda, S.Ninomiya, T.Seki, T.Aoki, J.Matsuo, Matrix-free high-resolution imaging mass spectrometry with high-energy ion projectiles, *J. Mass Spectrom.* **44** (2009) 128-136
- 105 B.N.Jones, V.Palitsin, R.P.Webb, Surface analysis with high energy time-of-flight secondary ion mass spectrometry measured in parallel with PIXE and RBS, *Nucl. Instr. Methods B*, **268** (2010) 1714-1717
- 106 B.N.Jones, J.Matsuo, Y.Nakata, H.Yamada, J.Watts, S.Hinder, V.Palitsin, R.P.Webb, *Surface & Interface Analysis*, **43** (2011) 249-252
- 107 W.Sichteremann, A.Benninghoven, Secondary ion formation from amino-acids by proton and cation transfer, *Int. J. Mass Spectrom. & Ion Processes.* **40** (1981) 177-184
- 108 Y.Wakamatsu, H.Yamada, S.Ninomiya, B.N.Jones, T.Seki, T.Aoki, R.P.Webb, J.Matsuo, Biomolecular Emission by Swift Heavy Ion Bombardment, *Ion Implantation Technology* (AIP: **CP1321**, 2010, edited by J. Matsuo, M. Kase, T. Aoki, and T. Seki) 233-236
- 109 M.F.Russo Jr., B.J.Garrison, Mesoscale Energy Deposition Footprint Model for Kilolectronvolt Cluster Bombardment of Solids, *Anal. Chem.* **78** (2006) 7206-7210
- 110 M.J.Bailey, B.N.Jones, S.Hinder, J.Watts, S.Bleay, R.P.Webb, Depth profiling of fingerprint and ink signals by SIMS and MeV SIMS, *Nucl. Instr. Methods B*, **268** (2010) 1929-1932
- 111 H.Yamada, Y.Nakata, S.Ninomiya, T.Seki, T.Aoki, J.Tamura, J.Matsuo, MeV-energy probe SIMS imaging of major components in washed and fractured animal cells, *Surface & Interface Analysis*, **43** (2011) 363-366
- 112 M.B.H.Breese, P.J.C.King, G.W.Grime, F.Watt, Micro-circuit imaging using an ion-beam-induced charge, *J.App.Phys.*, **72** (1992) 2097-2104
- 113 Z.He, Review of the Shockley Ramo Theorem and its applications in semiconductor gamma ray detectors, *Nucl. Instr. Methods A*, **463** (2001) 250-267

- 114 A.Lo Guidice, Y.Garino, C.Manfredotti, V.Rigato, E.Vittoni, Angle resolved IBIC analysis of 4H-SiC Schottky diodes, *Nucl. Instr. Methods B*, **249** (2006) 213-216
- 115 M.C.Veale, P.J.Sellin, J.Parkin, A.Lohstroh, A.W.Davies, P.Seller, Ion Beam Induced Charge Studies of CdZnTe Grown by Modified Vertical Bridgman Method, *IEEE Trans.Nucl.Sci.* **55** (2008) 3741-3745
- 116 Ž.Pastuović, E. Vittone, I.Capan, M.Jakšić, Probability of divacancy trap production in silicon diodes exposed to focused ion beam irradiation, *Appl. Phys. Lett.*, **98** (2011) 092101
- 117 M.B.H.Breese *et al.*, *J. Appl. Phys.*, **72** (1992 : see [112])
- 118 M.Zmeck, L.J.Balk, T.Osiewicz, F.Watt, J.C.H.Phang, A.M.Khambadkone, F.-J.Niedernostheide, H.-J.Schulze, Ion beam induced charge microscopy studies of power diodes. *J. Phys. Condens. Matter.*, **16** (2004) S57-S66
- 119 G.Vizkelethy, D.K.Brice, B.L.Doyle, The theory of ion beam induced charge in metal-oxide semiconductor structures, *J. Appl. Phys.* **101** (2007) 074506
- 120 J. Morse, M.Salomé, E.Berdermann, M.Pomorski, W.Cunningham, J.Grant, Single crystal CVD diamond as an X-ray beam monitor, *Diamond Relat. Materials*, **16** (2007) 1049-1052
- 121 J.Bohon, E.Muller, J.Smedley, Development of diamond-based X-ray detection for high flux beamline diagnostics, *Journal of Synchrotron Radiation*, **17** (2010) 711-718
- 122 S.Camarda, A.E.Bolotnikov, Y.Cui, A.Hossain, S.Awadalla, J.MacKenzie, H.Chen, R.B.James, Polarization Studies of CdZnTe Detectors Using Synchrotron X-ray Radiation, *IEEE Trans. Nucl. Sci.* **55** (6) (2008) 3725-3730
- 123 H.G.J.Moseley, The high frequency spectra of the elements, *Philos. Mag. Series 6*, **26** (1913) 1024-1034
- 124 H.G.J.Moseley, The high-frequency spectra of the elements. Part II, *Philos.Mag.Series 6*, **27** (1914) 703-713
- 125 J.Chadwick, The excitation of γ -rays by α -rays, *Philos.Mag.Series 6*, **25** (1913) 193-197
- 126 C.G.Barkla, The spectra of the fluorescent Röntgen radiations, *Philos.Mag.Series 6*, **22** (1911) 396-412
- 127 Harry R. Bowman, Earl K. Hyde, Stanley G. Thompson and Richard C. Jared, Application of High-Resolution Semiconductor Detectors in X-ray Emission Spectrography, *Science* **151** (1966) 562-568
- 128 T.B.Johansson, R.Akselsson, S.A.E.Johansson, X-ray analysis: Elemental trace analysis at the 10^{-12} g level, *Nucl. Instr. Methods* **84** (1970) 141-143
- 129 V.Valkovic, D.Miljanic, R.M.Wheeler, R.B.Liebert, T.Zabel, G.C.Phillips, Variation in trace metal concentrations along single hairs as measured by proton-induced X-ray-emission photometry, *Nature* **243** (1973) 543-544
- 130 W.Davidson, G.W.Grime, J.A.W.Morgan, K.Clarke, Distribution of dissolved iron in sediment pore waters at submillimeter resolution, *Nature* **352** (1991) 323-325
- 131 J.P.Landsberg, B.McDonald, F.Watt, Absence of aluminium in neuritic plaque cores in Alzheimers-disease, *Nature* **360** (1992) 65-68
- 132 adapted by R.Nave (downloaded 21st July 2011 from Georgia State University website), hyperphysics.phy-astr.gsu.edu/hbase/quantum/moseley.html
- 133 Hasegawa J, Tada T, Oguri Y, Hayashi M, Toriyama T, Kawabata T, Masai K, Development of a high-efficiency high-resolution particle-induced x-ray emission system for chemical state analysis of environmental samples, *Rev Sci Instrum* **78**(7) (2007) 073105
- 134 Kavčić M, Karydas AG, Zarkadas C, Chemical state analysis employing sub-natural linewidth resolution PIXE measurements of K alpha diagram lines, *X-Ray Spectrometry*, **34** (2005) 310-314
- 135 M.A.Reis, L.C.Alves, N.P.Barradas, P.C.Chaves, B.Nunes, A.Taborda, K.P.Surendran, A.Wu, P.M.Vilarinho, E.Alves, High Resolution and Differential PIXE combined with RBS, EBS and AFM analysis of MgTiO₃ multilayer structures, *Nucl. Instr. Methods B*, **268** (2010) 1980-1985
- 136 M.Kavčić, M.Zitnik, K.Bucar, J.Szlachetko, Application of wavelength dispersive X-ray spectroscopy to improve detection limits in X-ray analysis, *X-Ray Spectrometry*, **40**(1) (2011) 2-6
- 137 I.Orlic, F.Watt, K.K.Loh, S.M.Tang, Nuclear microscopy of single aerosol particles, *Nucl. Instrum. Methods B*, **85** (1994) 840-844
- 138 H. Paul, J. Sacher, Fitted empirical reference cross-sections for K-shell ionization by protons, *Atomic Data & Nuclear Data Tables*, **42** (1989) 105-156
- 139 M.A.Reis, A.P.Jesus, Semi-empirical approximation to cross-sections for L X-ray production by proton impact, *Atomic Data & Nuclear Data Tables*, **63** (1996) 1-55
- 140 A.Taborda, P.C.Chaves, M.A.Reis, Polynomial approximation to universal ionisation cross-sections of K and L shells induced by H and He ion beams, *X-Ray Spectrometry*, **40** (2011) 127-134
- 141 Gregory Lapicki, Javier Miranda, Updated database for L x-ray production by protons and extraction of L-subshell ionization cross sections from only $L\gamma$ and $La + L\beta$ cross sections, *X-ray Spectrometry* **40** (2011) 122-126
- 142 J.L.Campbell, N.I.Boyd, N.Grassi, P.Bonnick, J.A.Maxwell, The Guelph PIXE software package IV, *Nucl. Instrum. Methods B*, **268** (2010) 3356-3363
- 143 Christian Doppler, Über das farbige Licht der Doppelsterne und einiger anderer Gestirne des Himmels, *Proceedings of the Bohemian Society of Sciences* (1843). Doppler published this privately in 1842
- 144 John Scott Russell (1848), "On certain effects produced on sound by the rapid motion of the observer", *Report of the 18th Meeting of the British Association for the Advancement of Science* (John Murray: London) **18** (1849) 37-38
- 145 see W.Thomson, *Rep. Brit. Assoc.* **xcix** (1872)
- 146 N. Bohr, On the Constitution of Atoms and Molecules, *Philosophical Magazine* **26** (1913) 1-24
- 147 M.H.Chen, B.Crasemann, H.Mark., Relativistic K-shell Auger rates, level widths and fluorescence yields. *Phys. Rev. A*, **21** (1980) 436-441
- 148 M.H.Chen, B.Crasemann, H.Mark., Widths and fluorescence yields of atomic L vacancy states. *Phys. Rev. A*, **24** (1981) 177-182
- 149 M.H.Chen, B.Crasemann, H.Mark., Radiationless transitions to atomic $M_{1,2,3}$ shells: Results of relativistic theory. *Phys. Rev. A*, **27** (1983) 2989-2993
- 150 J.L.Campbell, Fluorescence yields and Coster-Kronig probabilities for the atomic L subshells, *Atomic Data and Nuclear Data Tables*, **85** (2003) 291-315
- 151 J.L.Campbell, Fluorescence yields and Coster-Kronig probabilities for the atomic L subshells. Part II: The L_1 subshell revisited, *Atomic Data and Nuclear Data Tables*, **95** (2009) 115-124

- 152 J.L.Campbell, P.L.McGhee, J.A.Maxwell, R.W.Ollerhead, B.Whittaker, Energy-dispersive measurements of the $K\alpha_3$, KM_1 , $K\beta_1$, and $K\beta_2$ x-ray intensities relative to the $K\alpha_1$ intensity in lead and uranium, *Phys. Rev. A* **33** (1986) 986-993
- 153 J.L.Campbell, J.-X.Wang, Interpolated Dirac-Fock values of L-subshell x-ray emission rates including overlap and exchange effects. *At. Data Nucl. Data Tables* **43** (1989) 281-291
- 154 M.H.Chen, B.Crasemann, M x-ray emission rates in Dirac-Fock approximation. *Phys. Rev. A* **30** (1984) 170-176
- 155 M.A.Reis, P.C.Chaves, A.Taborda, Radiative auger emission satellites observed by microcalorimeter-based energy-dispersive high-resolution PIXE, *X-Ray Spectrometry*, **40** (2011) 141-146
- 156 M.J.Berger, J.H.Hubbell, *NIST X-ray and Gamma-ray Attenuation Coefficients and Cross Sections Database, NIST Standard Reference Database 8, Version 2.0*, National Institute of Standards and Technology, Gaithersburg, MD (1990)
- 157 M.J.Berger, J.H.Hubbell, S.M.Seltzer, J.Chang, J.S.Coursey, R.Sukumar, D.S.Zucker, K.Olsen, K. (2010), *XCOM: Photon Cross Section Database* (v. 1.5). <http://physics.nist.gov/xcom> (downloaded 23 July 2011). National Institute of Standards and Technology, Gaithersburg, MD.
- 158 Farideh Jalilvand, University of Calgary : www.chem.ucalgary.ca/research/groups/faridehj/xas.pdf, downloaded 23 July 2011.
- 159 Burkhard Beckhoff, Reference-free X-ray spectrometry based on metrology using synchrotron radiation, *J. Anal. At. Spectrom.*, **23** (2008) 845-853
- 160 B.L.Henke, E.M.Gullikson, J.C.Davis, X-ray interactions -photoabsorption, scattering, transmission and reflection at $E=50-30,000$ eV, $Z=1-92$, *At. Data Nucl. Data Tables*, **54** (1993) 181-342
- 161 International Fundamental Parameters Initiative <http://exsa.pytalhost.net/FP-XRF> by EXSA <http://www.exsa.hu/> (downloaded 27 July 2011)
- 162 F.Rizzo, G.P.Cirrone, G.Cuttone, A.Esposito, S.Garraffo, G.Pappalardo, L.Pappalardo, F.P.Romano, S.Russo, Non-destructive determination of the silver content in Roman coins (nummi), dated to 308-311 AD, by the combined use of PIXE-alpha, XRF and DPAA techniques, *Microchemical Journal* **97** (2011) 286-290
- 163 D. Sokaras, A. G. Karydas, A. Oikonomou, N. Zacharias, K. Beltsios and V. Kantarelou, Combined elemental analysis of ancient glass beads by means of ion beam, portable XRF, and EPMA techniques, *Analytical and Bioanalytical Chemistry*, **395** (2009) 2199-2209
- 164 Michalski JR, Niles PB, Deep crustal carbonate rocks exposed by meteor impact on Mars, *Nature Geoscience* **3(11)** (2010) 751-755
- 165 A.N.Mansour, C.A.Melendres, Analysis of X-ray absorption spectra of some nickel oxycompounds using theoretical standards, *J.Phys.Chem.A*, **102** (1998) 65-81
- 166 E.Lombi, K.G.Scheckel, I.M.Kempson, *In-situ* analysis of metal(loid)s in plants: State of the art and artefacts, *Environmental & Experimental Botany*, **72** (2011) 3-17
- 167 M.P.Seah, S.J.Spencer, Ultrathin SiO₂ on Si. VII. Angular accuracy in XPS and an accurate attenuation length, *Surface & Interface Analysis* **37** (2005) 731-736
- 168 M.A.Reis, N.P.Barradas, P.C.Chaves, A.Taborda, PIXE analysis of multilayer targets, *X-ray Spectrometry* **40** (2011) 153-156
- 169 P.A.Mando, M.E.Fedi, N.Grassi, The present role of small particle accelerators for the study of Cultural Heritage, *European Physical Journal Plus* **126(4)** (2011) art.no.: 41
- 170 E.Rauhala, N.P.Barradas, S.Fazinić, M.Mayer, E.Szilágyi, M.Thompson, Status of ion beam data analysis and simulation software, *Nucl. Instrum. Methods B*, **244** (2006) 436-456
- 171 N.P.Barradas, K.Arstila, G.Battistig, M.Bianconi, N.Dytlewski, C.Jeynes, E.Kótai, G.Lulli, M.Mayer, E.Rauhala, E.Szilágyi, M.Thompson, IAEA intercomparison of IBA software, *Nucl. Instr. Methods B*, **262** (2007) 281-303
- 172 N.P. Barradas, K. Arstila, G. Battistig, M. Bianconi, N. Dytlewski, C. Jeynes, E. Kótai, G. Lulli, M. Mayer, E. Rauhala, E. Szilágyi and M. Thompson, "Summary of IAEA intercomparison of IBA software' ", *Nucl. Instr. Methods B*, **266** (2008) 1338-1342
- 173 M.Mayer, *Technical Report IPP9/113*, Max-Planck-Institut für Plasmaphysik, Garching, Germany, 1997
- 174 M.Mayer, SIMNRA, a simulation program for the analysis of NRA, RBS and ERDA, *AIP Conference Proceedings* **475** (1999) 541-544
- 175 M.Mayer, *SIMNRA version 5.0 User's Guide*, © Max-Planck-Institut für Plasmaphysik, 1997-2002 (156pp) www2.if.usp.br/~lamfi/guia-simnra.pdf (downloaded 25 July 2011)
- 176 C.Jeynes, N.P.Barradas, P.K.Marriott, G.Boudreault, M.Jenkin, E.Wendler, R.P.Webb, Elemental thin film depth profiles by IBA using simulated annealing - a new tool, *J. Phys. D Appl. Phys.*, **36** (2003) R97-R126
- 177 N.P.Barradas, C.Jeynes, Advanced physics and algorithms in the IBA DataFurnace, *Nucl. Instr. Methods B*, **266** (2008) 1875-1879
- 178 www.surreyibc.ac.uk/ndf (downloaded 25 July 2011)
- 179 C.J.Tavarez, L.Rebouta, E.Alves, N.P.Barradas, J.Pacaud, J.P.Rivière, Study of roughness in Ti_{0.4}Al_{0.6}N/Mo multilayer structures, *Nucl. Instr. Methods B*, **188** (2002) 90-95
- 180 W.H.Press, B.P.Flannery, S.A.Teukolsky, W.T.Vetterling, *Numerical Recipes*. Cambridge University Press, Cambridge, New York, 1988
- 181 N.P.Barradas, C.Jeynes, R.P.Webb, Simulated annealing analysis of RBS data, *Appl. Phys. Lett.* **71** (1997) 291-293
- 182 N.P.Barradas, C.Jeynes, M.Jenkin, P.K.Marriott, Bayesian error analysis of Rutherford backscattering spectra, *Thin Solid Films*, **343-344** (1999) 31-4
- 183 L.Wielopolski, R.P.Gardner, Prediction of pulse-height spectral distortion caused by peak pile-up effect, *Nucl. Instr. Methods*, **133** (1976) 303-309
- 184 N.P.Barradas, M.A.Reis, Accurate calculation of pileup effects in PIXE spectra from first principles, *X-ray Spectrometry*, **35(4)** (2006) 232-237
- 185 S.L. Molodtsov, A.F. Gurbich, Simulation of the pulse pile-up effect on the pulse-height spectrum, *Nucl. Instr. Methods B*, **267** (2009) 3484-3487
- 186 W.N.Lennard, G.R.Massoumi, Anomalous pulse heights in silicon detectors, *Nucl. Instr. Methods B*, **48** (1990) 47-50
- 187 C. Pascual-Izarra, N.P. Barradas, Introducing routine pulse height defect corrections in IBA, *Nucl. Instr. Methods B*, **266** (2008) 1866-1870

- 188 M.Mayer, Ion beam analysis of rough thin films, *Nucl. Instr. Methods B*, **194** (2002) 177–86
- 189 N.P.Barradas, Rutherford backscattering analysis of thin films and superlattices with roughness *J. Phys. D: Appl. Phys.* **34** (2001) 2109–16
- 190 S.L.Molodtsov, A.F.Gurbich, C.Jeynes, Accurate ion beam analysis in the presence of surface roughness, *J. Phys. D: Appl. Phys.* **41** (2008) 205303 (7pp)
- 191 Y.Sunitha, G.L.N.Reddy, SanjivKumar, V.S.Raju, Studies on interdiffusion in Pd/Mg/Si films: Towards improved cyclic stability in hydrogen storage, *Applied Surface Science* **256** (2009) 1553–1559
- 192 N.P.Barradas, Fitting of RBS data including roughness: application to Co/Re multilayers, *Nucl. Instr. Methods B*, **190** (2002) 247–51
- 193 J.P. Stoquert, T. Szörenyi, Determination of the number and size of inhomogeneities in thin films by ion beam analysis, *Phys. Rev. B* **66** (2002) 144108
- 194 M. Mayer, U. von Toussaint, J. Dewalque, O. Dubreuil, C. Henrist, R. Cloots, F. Mathis, Rutherford backscattering analysis of porous thin TiO₂ films, *Nucl. Instr. Methods B*, doi:10.1016/j.nimb.2011.07.045 (2011, **in press**)
- 195 N.P.Barradas, Calculation of the low energy yield in RBS, *Nucl. Instr. Methods B*, **261** (2007) 418–421
- 196 N.P.Barradas, Double scattering in grazing angle RBS spectra, *Nucl. Instr. Methods B*, **225** (2004) 318–330
- 197 E.Szilágyi, F. Pászti, G. Amsel, Theoretical approximations for depth resolution calculations in IBA methods, *Nucl. Instr. Methods B*, **100** (1995) 103–121
- 198 E.Szilágyi, Energy spread in ion beam analysis, *Nucl. Instr. Methods B*, **161–163** (2000) 37–47
- 199 Edit Szilágyi, The DEPTH code homepage. <http://www.kfki.hu/~ionhp/doc/prog/mdepth.htm> (downloaded 25 July 2011)
- 200 M.Mayer, RESOLNRA: A new program for optimizing the achievable depth resolution of ion beam analysis methods, *Nucl. Instr. Methods B*, **266** (2008) 1852–1857
- 201 François Schiettekatte, Fast Monte Carlo for IBA simulations, *Nucl. Instr. Methods B*, **266** (2008) 1880–1885
- 202 François Schiettekatte, The CORTEO code homepage: www.lps.umontreal.ca/~schiette/index.php?n=Recherche.Corteo (downloaded 26th July 2011)
- 203 K.Arstila, T.Sajavaara, J.Keinonen, Monte Carlo simulation of multiple and plural scattering in elastic recoil detection, *Nucl. Instr. Methods B*, **174** (2001) 163–172
- 204 I.Vickridge, G.Amsel, SPACES: A PC implementation of the stochastic theory of energy loss for narrow-resonance depth profiling, *Nucl. Instr. Methods B*, **45** (1990) 6–11
- 205 Link on SPIRIT website (downloaded 26 July 2011) <http://www.spirit-ion.eu/Techniques/IBA-software.html>
- 206 N.P.Barradas, R.Mateus, M.Fonseca, M.A.Reis, K.Lorenz, I.Vickridge, Thin film depth profiling using simultaneous particle backscattering and nuclear resonance profiling, *Nucl. Instr. Methods B*, **268** (2010) 1829–1832
- 207 H.W.Lewis, Straggling Effects on Resonant Yields, *Phys. Rev.* **125** (1962) 937–940
- 208 J.A.Maxwell, J.L.Campbell, W.J.Teesdale, The Guelph PIXE software package, *Nucl. Instr. Methods B*, **43** (1989) 218–230
- 209 K.Ishii, S.Morita, Continuum x-rays produced by light-ion – atom collisions, *Phys.Rev.A*, **30** (1984) 2278–2286
- 210 J.L.Campbell, W.Maenhaut, E.Bombelka, E.Clayton, K.Malmqvist, J.A..Maxwell, J.Pallon, J.Vandenhaute, An intercomparison of spectral data processing techniques in PIXE, *Nucl. Instr. and Methods B*, **14** (1986) 204–220
- 211 J.L.Campbell, J.A.Maxwell, S.M.Andrushenko, S.M.Taylor, B.N.Jones, W.Brown-Bury, A GUPIX-based approach to interpreting the PIXE-plus-XRF spectra from the Mars Exploration Rovers: I. Homogeneous Standards, *Nucl. Instr. Methods B*, **269(1)** (2011) 57–68
- 212 J.L.Campbell, A.M.McDonald, G.M.Perrett, S.M.Taylor, A GUPIX-based approach to interpreting the PIXE-plus-XRF spectra from the Mars Exploration Rovers: II Geochemical Reference Materials, *Nucl. Instr. Methods B*, **269(1)** (2011) 69–81
- 213 GeoPIXE home page, downloaded 26 July 2011: <http://nmp.csiro.au/GeoPIXE.html>
- 214 C.G.Ryan, D.R.Cousens, S.H.Sie, W.L.Griffin, G.F.Suter, E.Clayton, Quantitative pixe microanalysis of geological material using the CSIRO proton microprobe, *Nucl. Instr. Methods B*, **47** (2000) 55–71
- 215 C.G.Ryan, D.N.Jamieson, C.L.Churms, J.V.Pilcher, A new method for on-line true-elemental imaging using PIXE and the proton microprobe, *Nucl. Instr. Methods B*, **104** (2005) 157–165
- 216 C.G.Ryan, R.Kirkham, R.M.Hough, G.Moorhead, D.P.Siddons, M.D. de Jonge, D.J.Paterson, G.De Geronimo, D.L.Howard, J.S.Cleverley, Elemental X-ray imaging using the Maia detector array: The benefits and challenges of large solid-angle, *Nucl. Instr. Methods A*, **619** (2010) 37–43
- 217 J. Pallon, C.G. Ryan, N. Arteaga Marrero, M. Elfman, P. Kristiansson, E.J.C. Nilsson, C. Nilsson, STIM evaluation in GeoPIXE to complement the quantitative dynamic analysis, *Nucl. Instr. Methods B*, **267** (2009) 2080–2084
- 218 J.Boman, J.Isakson, Comparison between two x-ray analysis software packages, *X-ray Spectrometry* **20** (1991) 305–314
- 219 B.Vekemans, K.Janssens, L.Vincze, F.Adams, P.Van Espen, Analysis of X-ray spectra by iterative least squares (AXIL): New developments, *X-ray Spectrometry* **23** (1991) 278–285
- 220 K.Janssens, B.Vekemans, F.Adams, P.van Espen, P.Mutsaers, Accurate evaluation of μ PIXE and μ XRF spectral data through iterative least squares fitting, *Nucl. Instr. Methods B*, **109** (1996) 179–185
- 221 IAEA X-Ray Fluorescence Laboratory: "Quantitative X-ray Analysis System" (QXAS) and AXIL tools available www.iaea.org/OurWork/ST/NA/NAAL/pci/ins/xrf/pciXRFdown.php (downloaded 26 July 2011)
- 222 WinAxil X-Ray Analysis Software (S-5005) <http://www.canberra.com/products/438012.asp> (downloaded 26 July 2011)
- 223 G.W.Grime, M.Dawson, Recent developments in data acquisition and processing on the Oxford scanning proton microprobe, *Nucl. Instr. Methods B*, **104** (1995) 107–113
- 224 C.Pascual-Izarra, M.A.Reis, N.P.Barradas, Simultaneous PIXE and RBS data analysis using Bayesian inference with the DataFurnace code, *Nucl. Instr. Methods B*, **249** (2006) 780–783
- 225 C.Pascual-Izarra, N.P.Barradas, M.A.Reis, LibCPIXE: A PIXE simulation open-source library for multilayered samples, *Nucl. Instr. Methods B*, **249** (2006) 820–822

- 226 M.A.Reis, L.C.Alves, A.P.Jesus, Matrix effects correction for quantitative TPIXE analysis, *Nucl. Instr. Methods B*, **109-110** (1996) 134-138
- 227 M.A.Reis, P.C.Chaves, L.C.Alves, N.P.Barradas, DT2, a PIXE spectra simulation and fitting package, *X-Ray Spectrometry*, **37** (2008) 100-102
- 228 A.Mantero, H.Ben Abdelouahed, C.Champion, Z.El Bitar, Z.Francis, P.Guèye, S.Incerti, V.Ivanchenko M.Maire, PIXE simulation in Geant4, *X-Ray Spectrometry*, **40(1)** (2011) 2-6
- 229 M.Blaauw, J.L.Campbell, S.Fazinić, M.Jakšić, I.Orlić, P.Van Espen, The 2000 IAEA intercomparison of PIXE spectrum analysis software, *Nucl. Instr. Methods B*, **189** (2002) 113-122
- 230 IAEA-TECDOC-1342: *Intercomparison of PIXE spectrometry software packages* (IAEA, Vienna, 2003)
- 231 M.J.Bailey, S.Coe, D.M.Grant, G.W.Grime, C.Jeynes, Accurate determination of the Ca:P ratio in rough hydroxyapatite samples by SEM-EDS, PIXE and RBS—a comparative study, *X-Ray Spectrometry*, **38(4)** (2009) 343–347
- 232 N.P.Barradas, A.Vieira, R.Patricio, Artificial neural networks for automation of RBS experiments and data analysis, *Phys. Rev.E* **65(6)** (2002) 066703
- 233 M.M.Li, W.Guo, B.Verma, K.Tickle, J.O'Connor, Intelligent methods for solving inverse problems of backscattering spectra with noise: a comparison between neural networks and simulated annealing, *Neural Computing & Applications* **18(5)** (2009) 423-430
- 234 J.Demeulemeester, D.Smeets, N.P.Barradas, A.Vieira, C.M.Comrie, K.Temst, A.Vantomme, Artificial neural networks for instantaneous analysis of real-time RBS spectra, *Nucl. Instr. Methods B*, **268** (2010) 1676–1681
- 235 N.P. Barradas, A.Vieira, R.Patricio, RBS without humans, *Nucl. Instr. Methods B*, **190** (2002) 231-236
- 236 *Guide to the Expression of Uncertainty in Measurement*, International Organization for Standardization, Geneva, Switzerland, 1995, ISBN 92-67-10188-9
- 237 K.A.Sjöland, F.Munnik, U.Wätjen, Uncertainty budget for IBA, *Nucl. Instr. Methods B*, **161** (2000) 275-280
- 238 Seah M P, David D, Davies J A, Jeynes C, Ortega C, Sofield C, Weber G, An inter-comparison of absolute measurements of the oxygen and tantalum thickness of Ta₂O₅ reference materials BCR 261 by six laboratories, *Nucl. Instr. Methods B*, **30** (1988) 140–51
- 239 M.P.Seah, S.J.Spencer, F.Bensebaa, I.Vickridge, H.Danzebrink, M.Krumrey, T.Gross, W.Oesterle, E.Wendler, B. Rheinländer, Y.Azuma, I.Kojima, N.Suzuki, M.Suzuki, S.Tanuma, D.W.Moon, H.J.Lee, Hyun Mo Cho, H.Y.Chen, A.T.S.We, T.Osipowicz, J.S.Pan, W.A.Jordaan, R.Hauert, U.Klotz, C. van der Marel, M.Verheijen, Y.Tamm-inga, C.Jeynes, P.Bailey, S.Biswas, U.Falke, N.V.Nguyen, D.Chandler-Horowitz, J.R.Ehrstein, D.Muller, J.A.Dura, Critical review of the current status of thickness measurements for ultrathin SiO₂ on Si Part V: Results of a CCQM pilot study, *Surf. Interface Anal.* **36** (2004) 1269–1303
- 240 U.Wätjen, H.Bax, Bi-implanted silicon reference material revisited: uniformity of the remaining batch, *Nucl. Instr. Methods B*, **85** (1994) 627–32
- 241 K.H.Ecker, U.Wätjen, A.Berger, L.Persson, W.Pritzcow, M.Radtke, H.Riesemeier, RBS, SY-XRF, INAA and ICP-IDMS of antimony implanted in silicon—a multi-method approach to characterize and certify a reference material, *Nucl. Instr. Methods B*, **188** (2002) 120-125.
- 242 G.Boudreault, C.Jeynes, E.Wendler, A.Nejim, R.P.Webb, U.Wätjen, Accurate RBS measurement of ion implant doses in a silicon, *Surf.Interface Anal.*, **33** (2002) 478-486
- 243 C.Jeynes, N.Peng, N.P.Barradas, R.M.Gwilliam, Quality assurance in an implantation laboratory by high accuracy RBS, *Nucl. Instr. Methods B*, **249** (2006) 482–485
- 244 C.Jeynes & N.P.Barradas, "Pitfalls in ion beam analysis", Chapter 15 in *2010 Handbook of Modern IBA* (Y.Q.Wang & M.Nastasi, eds, 2nd Edition, Pittsburgh: MRS)
- 245 Helmut Paul, private communication 1st July 2011
- 246 A.L.Turkevich *et al*, *Science* **158**, 1967 (see [21])
- 247 C.Jeynes, Z.H.Jafri, R.P.Webb, A.C.Kimber, M.J.Ashwin, Accurate RBS Measurements of the Indium Content of In-GaAs Thin Films, *Surf.Interface Anal.* **25** (1997) 254–260
- 248 Fischer R, Mayer M, von der Linden W, Dose V, Enhancement of the energy resolution in ion-beam experiments with the maximum-entropy method, *Phys. Rev. E* **55** (1997) 6667–3
- 249 M.Kopecek, L.Bacakova, J.Vacik, F.Fendrych, V.Vorlicek, I.Kratochvilova, V.Lisa, E.Van Hove, C.Mer, P.Bergonzo, M.Nesladek, Improved adhesion, growth and maturation of human bone-derived cells on nanocrystalline diamond films, *physica status solidi (a)* **205** (2008) 2146–2153
- 250 Siketić Z, Radović IB, Alves E, Barradas NP, Stopping power of ¹¹B in Si and TiO₂ measured with a bulk sample method and Bayesian inference data analysis, *Nucl. Instr. Methods B*, **268(11-12)** (2010) 1768-1771
- 251 E.Rauhala, Proton elastic scattering cross sections of C, N and Si for backscattering analysis in the energy range 0.7–2.5 MeV, *Nucl. Instr. Methods B*, **12(4)** (1985) 447-452
- 252 R. Salomonović, Angular distribution of proton non-Rutherford elastic scattering cross section of carbon and silicon, *Nucl. Instr. Methods B*, **82(1)** (1993) 1-6
- 253 Barradas NP, Ramos AR, Alves E, Determination of non-Rutherford cross-sections from simple EBS spectra using Bayesian inference data analysis, *Nucl. Instr. Methods B*, **266(8)** (2008) 1180-1184
- 254 Giulia Calzolari, Massimo Chiari, Franco Lucarelli, Federico Mazzei, Silvia Nava, Paolo Prati, Gianluigi Valli, Roberta Vecchi, PIXE and XRF analysis of particulate matter samples: an inter-laboratory comparison, *Nucl. Instr. Methods B*, **266** (2008) 2401–2404
- 255 G.W. Grime, The "Q factor" method: quantitative microPIXE analysis using RBS normalisation, *Nucl. Instr. Methods B*, **109-110** (1996) 170-174
- 256 I. Orlić, Shijun Zhou, J.L. Sanchez, F. Watt, S.M Tang, Virtual PIXE and RBS laboratory, *Nucl. Instr. Methods B*, **150** (1999) 83-89
- 257 H.Bureau, C.Raepsaet, H.Khodja, ACarraro, C.Aubaud, Determination of hydrogen content in geological samples using elastic recoil detection analysis, *Geochimica et Cosmochimica Acta* **73(11)** (2009) 3311-3322
- 258 J.Lao, J.M.Nedelec, E.Jallot, New insight into the physicochemistry at the interface between sol-gel-derived bioactive glasses and biological medium: A PIXE-RBS study, *J. Phys. Chem C*, **112(25)** (2008) 9418-9427
- 259 Rajendran R, Ren MQ, Ynsa MD, Casadesus G, Smith MA, Perry G, Halliwell B, Watt F, A novel approach to the identification and quantitative elemental analysis of amyloid deposits—Insights into the pathology of Alzheimer's disease, *Biochemical & Biophysical Res. Comm.* **382(1)** (2000) 91-95

- 260 M.Arroyo-Hernandez, M.Manso-Silvan, E.Lopez-Elvira, A.Munoz, A.Climent, J.M.Martinez Duart, One step processing of aminofunctionalized gate oxides, *Biosensors & Bioelectronics*, **22(12)** (2007) 2786-2789
- 261 R.Huszank, A.Simon, E.Szilágyi, K.Keresztessy, I.Kovács, Micro-ERDA, micro-RBS and micro-PIXE techniques in the investigation of fish otoliths, *Nucl. Instr. Methods B*, **267** (2009) 2132–2135
- 262 L.de Viguerie, L.Beck, J.Salomon, L.Pichon, Ph.Walter, Composition of Renaissance paint layers: simultaneous PIXE and BS, *Anal. Chem.*, **81** (2009) 7960-7966
- 263 M.A.Reis, L.C.Alves, N.P.Barradas, P.C.Chaves, B.Nunes, A.Taborda, K.P.Surendran, A.Wu, P.M.Vilarinho, E.Alves, High Resolution and Differential PIXE combined with RBS, EBS and AFM analysis of MgTiO₃ multilayer structures, *Nucl. Instr. Methods B*, **268(11-12)** (2010) 1980-1985
- 264 G.Demortier, F.Bodart, Complementarity of PIXE and PIGE for the characterization of gold items of ancient jewelry, *J.Radioanal.Chem.* **69** (1982) 239-257
- 265 F.Lucarelli, S.Nava, G.Calzolai, M.Chiari, R.Udisti, F.Marino, Is PIXE still a useful technique for the analysis of atmospheric aerosols? The LABEC experience, *X-Ray Spectrometry*, **40(1)** (2011) 162-167
- 266 Elspeth F. Garman, Geoffrey W. Grime, Elemental analysis of proteins by microPIXE, *Progress in Biophysics and Molecular Biology* **89** (2005) 173–205
- 267 S.C.Willies, M.N.Isupov, E.F.Garman, J.A.Littlechild, The binding of haem and zinc in the 1.9 Å X-ray structure of Escherichia coli bacterioferritin, *J. Biol. Inorg. Chem.* **14(2)** (2009) 201-207
- 268 C.Pascual-Izarra, N.P.Barradas, M.A.Reis, C.Jeynes, M.Menu, B.Lavedrine, J.J.Ezrati, S.Röhrs, Towards truly simultaneous PIXE and RBS analysis of layered objects in cultural heritage, *Nucl. Instr. Methods B*, **261** (2007) 426-429
- 269 L.Beck, C.Jeynes, N.P.Barradas, Characterization of paint layers by simultaneous self-consistent fitting of RBS/PIXE spectra using simulated annealing, *Nucl. Instr. Methods B*, **266** (2008) 1871-1874
- 270 J.C.G.Jeynes, C.Jeynes, K.J.Kirkby, M.Rümmeli, S.R.P.Silva, RBS/EBS/PIXE measurement of single-walled carbon nanotube modification by nitric acid purification treatment, *Nucl. Instr. Methods B*, **266** (2008)1569-1573
- 271 V. Corregidor, P. C. Chaves, M. A. Reis, C. Pascual-Izarra, E Alves and N. P Barradas, Combination of IBA techniques for composition analysis of GaIn AsSb films, *Mat. Sci. Forum*, **514-516** (2006) 1603-1607
- 272 Chris Jeynes, G.Zoppi, I.Forbes, M.J.Bailey, N.Peng, Characterisation of thin film chalcogenide PV materials using MeV IBA, *IEEE Proc. SuperGen Conf.*, Nanjing, April 2009, DOI:10.1109/SUPERGEN.2009.5348162
- 273 M.A.Reis, N.P.Barradas, C.Pascual-Izarra, P.C.Chaves, A.R.Ramos, E.Alves, G.Gonzalez-Aguilar, M.E.V.Costa, I.M.M.Salvado, Holistic RBS-PIXE data reanalysis of SBT thin film samples, *Nucl. Instr. Methods B*, **261** (2007) 439-442
- 274 L.Beck, P.C.Gutiérrez, J.Salomon, Ph.Walter, M.Menu, in: *Proceedings of the XI International Conference on PIXE and its Analytical Applications, Puebla, Mexico, May 25–29, 2007*. ISBN 978-970-32-5115-5.
- 275 M.J. Bailey, Surface analysis techniques in forensic science (introduction to Forensics Special Issue), *Surf.Interface Anal.*, **42(5)** (2010) 339–340
- 276 M.J. Bailey, K.J.Kirkby, C.Jeynes, Trace element profiling of gunshot residues by PIXE and SEM-EDS: a feasibility study, *X-Ray Spectrometry*, **38(3)** (2009) 190-194
- 277 M.J.Bailey, C.Jeynes, Characterisation of gunshot residue particles using self-consistent ion beam analysis, *Nucl. Instr. Methods B*, **267** (2009) 2265-2268
- 278 M.J.Bailey, K.T.Howard, K.J.Kirkby, C.Jeynes, Characterisation of inhomogeneous inclusions in Darwin glass using IBA, *Nucl. Instr. Methods B*, **267** (2009) 2219–2224
- 279 C.Jeynes, M.J.Bailey, N.J.Bright, M.E.Christopher, G.W.Grime, B.N.Jones, V.V.Palitsin, R.P.Webb, "Total IBA" – where are we? *Nucl. Instr. Methods B*, **271** (2012) 107-118
- 280 B.L.Doyle, P.P.Provencio, P.G.Kotula, A.J.Antolak, C.G.Ryan, J.L.Campbell, K.Barrett, PIXE-quantified AXSIA: Elemental mapping by multivariate spectral analysis, *Nucl. Instr. Methods B*, **249** (2006) 828-832
- 281 M.R.Keenan, Exploiting spatial-domain simplicity in spectral image analysis, *Surf. Interface Anal.* **41** (2009) 79-87
- 282 David N. Jamieson New generation nuclear microprobe systems, *Nucl. Instr. Methods B*, **181** (2001) 1-11
- 283 M.J.Merchant, G.W.Grime, K.J.Kirkby, R.Webb, A survey of two-stage focusing systems for nanobeam design, *Nucl. Instr. Methods B*, **260** (2007) 8-14
- 284 O.Hagiwara, M.Watanabe, E.Sato, H.Matsukiyo, A.Osawa, T.Enomoto, J.Nagao, S.Sato, A.Ogawa, J.Onagawa, Energy-discrimination X-ray computed tomography system utilizing a silicon-PIN detector and its application to 2.0-keV-width K-edge imaging, *Nucl. Instr. Methods B*, **638(1)** (2011) 165-170
- 285 C.E.Killian, R.A.Metzler, Y.T.Gong, T.H.Churchill, I.C.Olson, Trubetskoy, M.B.Christensen, J.H.Fournelle, F.De Carlo, S.Cohen, J.Mahamid, A.Scholl, A.Young, A.Doran, F.H.Wilt, S.N.Coppersmith, P.U.P.A.Gilbert, Self-Sharpening Mechanism of the Sea Urchin Tooth, *Advanced Functional Materials*, **21(4)** (2011) 682-690
- 286 I.Gomez-Morilla, T.Pinheiro, S.Odenbach, M.D.Y.Alcala, X-ray tomography as a complementary technique to nuclear microscopy for biomedical applications, *Nucl. Instr. Methods B*, **267** (2009) 2103-2106
- 287 T.Satoh, M.Oikawa, T.Kamiya, Three-dimensional measurement of elemental distribution in minute samples by combination of in-air micro-PIXE and STIM, *Nucl. Instr. Methods B*, **267** (2009) 2125-2127
- 288 C.G.Ryan, PIXE and the nuclear microprobe: Tools for quantitative imaging of complex natural materials, *Nucl. Instr. Methods B*, **269** (2011) 2151-2162
- 289 T.Andrea, M.Rothermel, R.Werner, T.Butz, T.Reinert, Limited angle STIM and PIXE tomography of single cells, *Nucl. Instr. Methods B*, **268** (2010) 1884–1888
- 290 Jeroen A. van Kan, A.A.Bettiol, F.Watt, Proton Beam Writing of Three-Dimensional Nanostructures in Hydrogen Silsesquioxane, *Nano Letters* **6** (2006) 579-582
- 291 Jeroen A. Van Kan, A.A.Bettiol, K.Ansari, Ee Jin Teo, Tze Chien Sum, F.Watt, Proton beam writing: a progress review, *Int. J. Nanotechnology*, **1** (2004) 464-479
- 292 M. Mayer, W. Eckstein, H. Langhuth, F. Schiettekatte, U. von Toussaint, Computer simulation of ion beam analysis: Possibilities and limitations, *Nucl. Instr. Methods B*, **269** (2011) 3006-3013